minerals

MDPI

Article

Hydrothermal Scheelite Associated with Upper Cretaceous Intrusions in Romania: A Mineralogical Insight to the W Metallogeny

Ştefan Marincea [1,*], Delia-Georgeta Dumitraş [1], Cristina Sava Ghineț [1], George Dincă [1], Aurora-Măruța Iancu [1], Frédéric Hatert [2], Martin Depret [2] and Gelu Costin [3]

[1] Department INI, Geological Institute of Romania, 1 Caransebeş Str., RO-012271 Bucharest, Romania; d_deliaro@yahoo.com (D.-G.D.); ghinet.cristina@yahoo.com (C.S.G.); georgedinca@rocketmail.com (G.D.); iancu.maruta@yahoo.com (A.-M.I.)

[2] Laboratoire de Minéralogie, Université de Liège, Sart-Tilman, Bâtiment B 18, B-4000 Liège, Belgium; fhatert@uliege.be (F.H.); martin.depret@uliege.be (M.D.)

[3] Department of Earth, Environmental and Planetary Sciences, Rice University, Houston, TX 77005, USA; g.costin@rice.edu

* Correspondence: smarincea@yahoo.com or marincea@igr.ro

Abstract

Hydrothermal scheelite from three Romanian occurrences was analyzed in order to ascertain its structural, physical, vibrational, paragenetic, and crystal-chemical peculiarities as an important tool for characterizing the metallogenetic behavior and facilitating the ore-processing. All three occurrences, i.e., Ciclova and Oravița in Banat and Băița Bihor in the Bihor Mountains, are related to skarn deposits developed at the contact of Upper Cretaceous granodioritic bodies with Mesozoic calcareous deposits. Typical crystals show {001}, {111}, and {101} forms and are up to 15 mm across. The structure was successfully refined as tetragonal, space group $I4_1/a$, with R_1 = 0.0165 (Ciclova), 0.0204 (Oravița), and 0.0237 (Băița Bihor), respectively. The cell parameters refined for the same samples are a = 5.2459(10) Å and c = 11.3777(5) Å at Ciclova, a = 5.2380(2) Å and c = 11.3679(8) Å at Oravița, and a = 5.2409(2) Å and c = 11.3705(6) Å at Băița Bihor. The multiplicity of bands in both infrared absorption and Raman spectra is consistent with the S_4 punctual symmetry of the tungstate anion, agreeing with the structural data. In all cases, the analyzed scheelite is close to the $CaWO_4$ end-member. Cathodoluminescence peculiarities at the level of single crystals suggest that they crystallized in a slightly oxidizing to reducing environment from late hydrothermal solutions. Textural and paragenetic peculiarities suggest that scheelite from the three occurrences crystallized from epithermal, low-temperature, fluoride- and boron-bearing aqueous solutions.

Keywords: hydrothermal scheelite; physical properties; crystal chemistry; X-ray powder diffraction data; single-crystal X-ray diffraction; structure; infrared and Raman spectra; Cu-W skarn deposits; Upper Cretaceous; Romania

Academic Editors: Alexander R Cruden and Claire E. Wade

Received: 11 June 2025
Revised: 8 August 2025
Accepted: 11 August 2025
Published: 13 August 2025

Citation: Marincea, Ş.; Dumitraş, D.-G.; Sava Ghineț, C.; Dincă, G.; Iancu, A.-M.; Hatert, F.; Depret, M.; Costin, G. Hydrothermal Scheelite Associated with Upper Cretaceous Intrusions in Romania: A Mineralogical Insight to the W Metallogeny. *Minerals* **2025**, *15*, 854. https://doi.org/10.3390/min15080854

1. Introduction

Scheelite, ideally $CaWO_4$, accounts for a significant source of tungsten. Present in about 65% of the tungsten deposits throughout the world, the mineral is of major economic importance (e.g., [1–3] and referred works). Due to its very significant economic importance and high supply risk, tungsten was listed as one of the 32 critical materials in Europe (e.g., [4]) and 50 in the USA (e.g., [5]) and is also considered a hi-tech metal [6]. As

such, tungsten is primarily used to make wear-resistant metals but also in manufacturing electrodes, heating elements, field emitters, filaments in light bulbs, and cathode ray tubes. The detailed mineralogical study of scheelite as a major source for tungsten is then of great importance, offering an important tool to facilitate ore processing. Scheelite itself is widely used in scintillators for X-ray and gamma-ray detection, whereas compounds with scheelite structure were found to have extra low thermal conductivity [7] and were also investigated as photoanodes [8], photocatalysts [9], or even for nuclear waste immobilization [10]. Last but not least, scheelite can be used, in special conditions, as an appreciated gemstone [11,12].

Reported for the first time at the beginning of the 20th century [13], scheelite from Romania characteristically occurs in skarn deposits, the best-known occurrences being those at Ciclova (e.g., [13,14]), Oravița [14,15], and Băița Bihor: [14,16]. In all three of these occurrences, complex characterization mineralogy is lacking. The goal of this study is to fill the gaps existing in the mineralogical knowledge of the Romanian scheelite associated with Upper Cretaceous intrusions, insisting on its structural, physical, vibrational, paragenetic, and crystal-chemical peculiarities, of real use not only for mineralogists but also for prospectors, ore processors, and metallurgists. Last but not least, we appreciate that scheelite could represent, at least at Băița Bihor, an important component of a complex tungsten ore.

2. Geological Setting

The Ciclova, Oravița, and Băița Bihor occurrences are related to proximal or distal skarns developed at/near the contact of granodiorite bodies ascribed to the so-called "Banatitic Magmatic and Metallogenetic Belt"—BMMB [17]. The BMMB consists of a series of discontinuous magmatic and metallogenetic districts that are discordant over a Middle Cretaceous-aged nappe structure ([18–22] and references therein). The intrusive bodies are ascribed to calc-alkaline hydrated magmas and belong to I-type/magnetite series granitoids, derived from a primitive monzodiorite parent with a deep crust or upper mantle source region. These magmatic complexes (high-K calc-alkaline to calc-alkaline) are all productive in terms of ore formation [17,23].

The formation and evolution of the BMMB was early ascribed to subduction models involving either slab-rollback or slab-tear mechanisms affecting the subduction front of the Vardar Ocean ([20] and references therein). Other authors regarded magmatites in BMMB as post-collisional type I magmatites and ascribed the abundance of ore deposits in the eastern part of the Alpine–Balkan–Carpathian–Dinarides (ABCD) realm to a slab break-off of subducted lithosphere fragments during the Vardar Ocean closure, which imposed the rolling back and steepening of slabs. This process leads to upper crust extension and favors the access of melts to high crustal levels. The Cenozoic collision between the Tisia and Dacia blocks might be responsible for overall crustal thickening, for the formation of extensional faults that facilitated magma upwelling, and for a clockwise rotation of 60–80° with respect to the initial east-west trend at the time of magmatic emplacement ([19,21,22], and references therein).

The locations of the three occurrences in the general context of BMMB are given in Figure 1.

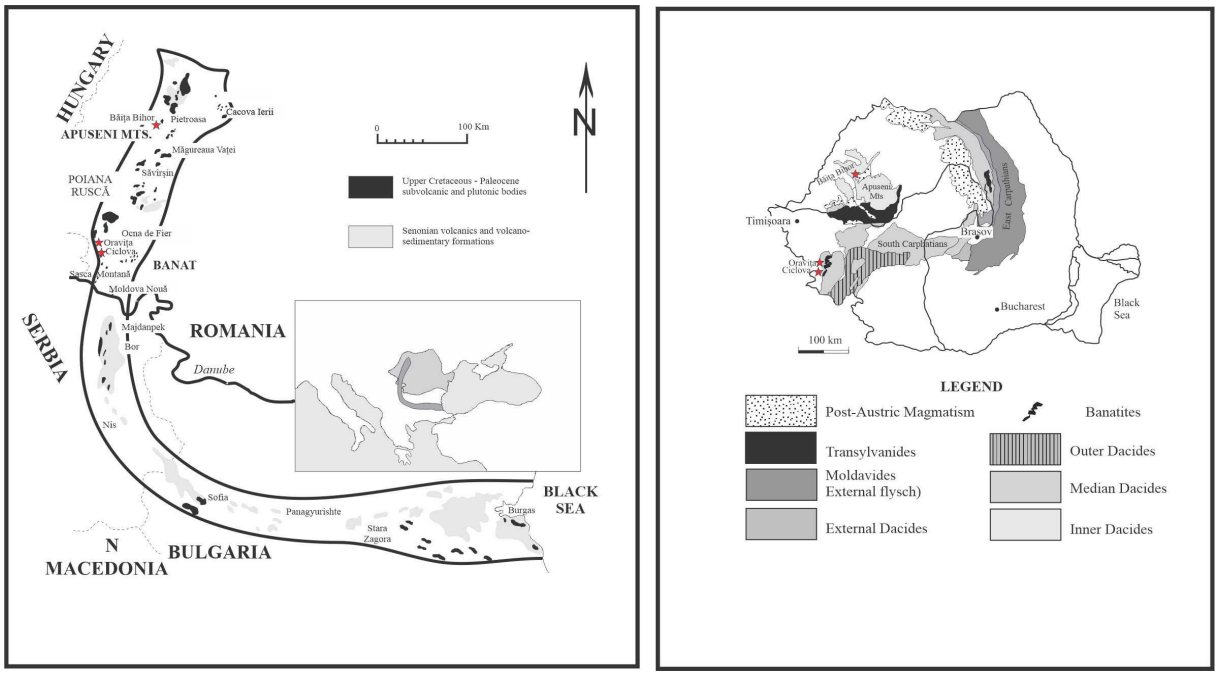

Figure 1. Sketch of the "Banatitic Magmatic and Metallogenetic Belt" ((**top left**): redrawn from [18]) showing its position in Europe (central detail, with BMMB painted in dark grey) and the structural context of Romania ((**top right**): from [24], simplified). The studied occurrences are marked with stars.

In all three occurrences, the granitoids were emplaced at shallow depths. Plutons show little evidence for differentiation, which is observed in other skarn systems (e.g., Fe, Au, and Zn skarns: [25]). Specific information on the analyzed bodies and on the skarn protolith is reported in Table 1.

Table 1. Geological features of the analyzed scheelite-bearing skarns.

Occurrence	Intrusion	Age of Intrusion	Protolith	Age of Protolith	Structural Unit
Ciclova Oraviţa	Ciclova-Oraviţa pluton	79 ± 3 to 74 ± 3 Ma [26] (1) 73.9 ± 3.2 to 71.2 ± 4.1 Ma [27] (2) 86.77 ± 0.5 to 87.70 ± 0.5 [20] (3)	carbonated veins in endoskarn	Mesozoic	Locva unit
Băiţa Bihor	Bihor batholith	77 ± 3 to 67 ± 3 Ma [28] (4) 70 ± 5 Ma [29] (5) 80.63 ± 0.3 to 78.69 ± 0.4 Ma [20] (3) 80.3 ± 1.6 Ma [27] (2)	dolostones	Anisian-Carnian; Carnian-Norian	Vălani unit; Vetre unit

(1) K-Ar on biotite; (2) U-Pb on zircon; (3) Re-Os data on molybdenite; (4) K-Ar ages on whole rock or on "femic" minerals; (5) Rb-Sr isochron.

Skarn deposits are one of the most representative types of mineralization from BMMB [17]. Copper metallogeny is predominant and distinguishes the BMMB in the context of the larger Alpine-Balkan–Carpathian–Dinaride belt [19]. A Cu-Mo zone can be distinguished in most of the Romanian deposits, including the Ciclova, Oravița, and Băița Bihor occurrences. Towards the external zones, Mo-rich ores grade into Mo-W-Bi-Te (in calcic skarns) or Cu-W-Bi (in magnesian skarns) [17,30,31].

Scheelite forms significant concentrations in the Cu-Mo (W) mineralization of Băița Bihor [30] and Oravița–Ciclova [15]. At Băiţa Bihor, scheelite occurs in distal magnesian skarns forming typical metasomatic columns whose outer zones contain magnesian borates (i.e., ludwigite, kotoite, suanite, fluoborite, and szaibélyite), whereas the inner zones typically contain magnesian silicates (e.g., diopside, forsterite, humite-group minerals, and

phlogopite) [32]. In this deposit, scheelite typically associates with chalcopyrite, galena, sphalerite, molybdenite, bornite, Bi-Cu sulphosalts, and Bi tellurides (e.g., [33,34]).

The scheelite occurrences from Ciclova and Oravița subscribe to vein systems developed at the level of endoskarn. The typical mineral association comprises, beside calcite, chalcopyrite, arsenopyrite, pyrite, gersdorffite, glaucodot, fluorite, and, according to [15], adularia, cobaltite, cubanite, molybdenite, and Bi-Cu sulphosalts.

3. Materials and Methods

The samples described in this paper were taken from three waste dumps pertaining to the Lobkowitz Gallery, located on Anton Brook in Ciclova (45°03′09″ N–21°44′25″ E); the Emil Gallery, located on Chinisea Valley in Oravița (45°04′42″ N–21°43′16″ E); and a collector located inside the Baia Roşie basal (transportation) Gallery, emergent on Crişul Negru Valley, in Băița Bihor (emergence: 46°29′14″ N–22°36′53″ E). Galleries from Ciclova and Oravița were mined for copper during the second half of the 19th century and reopened in the 50th year of the 20th century. The gallery at Băița Bihor is still active and is used for the Cu ore evacuation. The samples from Băița Bihor probably originate from Antoniu or Baia Roşie skarn bodies (metasomatic columns), where scheelite is particularly abundant [16].

Electron-microprobe analyses (EMPA) were performed using a Jeol JXA 8530F Hyperprobe (JEOL Ltd., Tokyo, Japan), equipped with a field emission-assisted thermo-ionic (Schottky) emitter, five wavelength-dispersive spectrometers (WDS), and one SD EDS detector. The apparatus is hosted by Rice University, Department of Earth, Environment, and Planetary Science (Houston, TX, USA). The apparatus was set at an accelerating voltage of 15 kV and a beam current of 20 nA (measured at the Faraday cup), for beam diameters of 5–10 μm. Natural chalcopyrite (Cu Kα), natural periclase (Mg Kα), natural hematite (Fe Kα), natural rhodonite (Mn Kα), natural scheelite (W Kα), natural molybdenite (Mo and S Kα), natural galena (Pb Kα), natural diopside (Ca Kα), metallic Bi (Bi Kα), and metallic Sb (Sb Kα) served as standards. Counting time was 20 s per element. Data were reduced using the Phi-Rho-Z matrix correction [35].

The fast identification of mineral phases in all samples was performed by Energy-Dispersive Spectrometry (EDS) analysis, using a JEOL Silicon Drift (SD) X-ray Detector with a 10 mm^2 active area and 133 eV resolution. The detector is attached and integrated into the JEOL JXA 8530F Hyperprobe described before. The analytical conditions used for EDS analysis were as follows: 15 kV accelerating voltage, 20 nA beam current, live time 20 s. Dead Time (DT) during the analysis was 35%–40% with count rates ranging from ~45,000 to ~100,000. The beam size used was "spot" size (~300 nm). Cathodoluminescence (CL) imaging was performed using a Gatan CL system (Gatan Inc., Pleasanton, CA, USA). Images were acquired at a voltage of 10 kV and contrast-enhanced for better observation.

X-ray powder diffraction (XRD) analysis of selected samples was performed on two different Brucker (AXS) D8 Advance diffractometers equipped with Bruker AXS Hi-star Area Detectors (Bruker, Karlsruhe, Germany) hosted by the Geological Institute of Romania (Bucharest) and by the University in Liège, Belgium, respectively. Both diffractometers used Ni-filtered Cu*Kα* radiation ($K\alpha_1$ = 1.54056 Å) with Cu anode Kristalloflex K780 X-ray tubes, a step size of 0.02° 2θ, and a counting time of 6 s per step. An operating voltage of 40 kV for a current of 30 mA, a slit system of 1/0.1/1 with a receiving slit of 0.6 mm, and a scanning range of 4 to 100° 2θ were used for all measurements. Unit-cell parameters were calculated by least-squares refinement of the XRD data, using the computer program of [36] modified for PC use by [37]. Synthetic silicon (NBS 640b) was used as an external standard in order to verify the accuracy of the measurements. As the sample grinding seems to lower the crystallinity of the mineral, as well as to produce its partial carbonation, as in the case

of Ca silicates [38], separate determinations of the unit-cell values were carried out based on single-crystal X-ray diffraction.

Structure refinements of scheelite crystals were performed by single-crystal X-ray diffraction on a Rigaku Agilent Xcalibur EOS diffractometer equipped with a CCD Detector (both manufactured in Osaka, Japan), housed at the Laboratory of Mineralogy, University of Liège. Data were collected at room temperature (293 K) with monochromatized Mo$K\alpha$ radiation (λ = 0.71703 Å) at 40 kV and 40 mA. The instrument has Kappa geometry (ϕ/ω scan). Data collection, subsequent data reduction, and face-based absorption corrections were carried out using the CrysAlis Pro 41.123a software [39]. The initial solution of the structure in space group $I4_1/a$ was determined by the charge flipping method using the Superflip algorithm [40], and the structural model was subsequently refined on the basis of F^2 with the Jana2006 software [41].

The infrared-absorption spectrum of a sample from Oravița was obtained at the Geological Institute of Romania with a SPECORD M-80 IR spectrophotometer (Carl Zeiss, Jena, Germany), using a conventional pressed disk technique. Carefully dried mineral powders were embedded in KBr; a dilution of 2.5 wt.% was used. This spectrum was recorded between 250 and 4000 cm^{-1}. FT-IR spectra of representative samples from Ciclova and Băița Bihor, as well as details of the stretching region of $(WO_4)^{2-}$ groups in the scheelite structure, were obtained using a BRUKER FTIR S 12 spectrometer (Ettlingen, Germany) also hosted by the Geological Institute of Romania. In this case, the records were made in the frequency range between 400 and 4000 cm^{-1}, using the standard pressed-disk technique, after embedding 2 mg of mechanically ground mineral powder in 148 mg of dry KBr and compacting at 2500 N/cm^2 pressure. The spectral resolution was 0.1 cm^{-1}. All spectra were recorded at 25 °C.

Raman spectra were recorded using a Renishaw SEM-Raman system (Artisan Scientific, Champaign, IL, USA) hosted by the Geological Institute of Romania, at 25 °C, using both structural and chemical analysis (SCA) and inVia interfaces. The spectrometer was equipped with a 10 mW, 532 nm diode-pumped solid-state laser as an excitation source. The spectral resolution was 1 cm^{-1} for a 1 μm spatial resolution. Analyses were collected using a 50× objective, a confocal aperture of 400 μm, a 150 μm slit width, and 1800 lines·mm^{-1} grating. The spectra were collected in the range of 10–1500 cm^{-1} (10-s accumulation time, 10 scans). The instrument was calibrated with synthetic silicon.

The mean density of various crystals of scheelite was measured using a pycnometer (Rainhard Co., Austin, TX, USA) at 25 °C, using a mixture of methylene iodide and toluene as the immersion liquid.

Indices of refraction were measured at room temperature (25 °C) using a conventional JENAPOL-U petrographic microscope (Carl Zeiss, Jena, Germany) with a spindle stage and calibrated immersion liquids (Cargille or temperature-calibrated oils), with a 589-nm interference filter. Thin-section photographs were obtained using a Zeiss Axio Imager A2M microscope (Carl Zeiss, Jena, Germany) with 2.5×/10×/20× objectives.

UV-luminescence tests were performed using a portable Vetter ultraviolet lamp (Vetter, Lottstetten, Germany) with 254 and 366 nm filters, respectively.

4. Mode of Occurrence and Morphology

At the macroscopic level, scheelite crystals occur as roughly tetragonal crystals up to 30 mm across, easily identified in UV light (Figure 2). At Oravița, the crystals are generally anhedral, due to secondary overgrowths (see below). Previous studies have described scheelite nodules up to 1 cm in diameter at Ciclova [15], as well as well-formed crystals having {001} (basal pinacoid), {111} (pyramid), and {101} (prism) forms [13]. At Băița Bihor,

euhedral to subhedral crystals vary in size from microns to 3 cm [16]. Twinning on {110} was rarely recognized, as were contact twins with a composition plane of (110).

Figure 2. Hand-specimen photographs of scheelite-bearing skarns from Ciclova ((**left**), Sample 2575) and Băiţa Bihor ((**right**), Sample 2591) showing the UV phosphorescence color. The coin diameter is 2 cm.

The microscopic study reveals that the mineral can occur as clusters or streaks of crystals, but also as individual crystals, as already observed by [16]. The crystals are generally subhedral or even anhedral at Oravița [15]. In most of the cases, partly preserved tetragonal contours can be observed (Figure 2). The distinct cleavage on {101} can be observed, as it is sometimes lined by secondary hydrotungstite.

The CL imaging at the electron microscope is relevant for the tetragonal symmetry of the mineral. Transversal sections of typical crystals of scheelite from Ciclova, Oravița, and Băița Bihor are given in Figure 3 and generally reveal oscillatory CL zoning suggesting the tetragonal symmetry. Overgrowths of secondary scheelite on previous crystals (Figure 3B,C) could explain the anhedral contours observed in some cases [15].

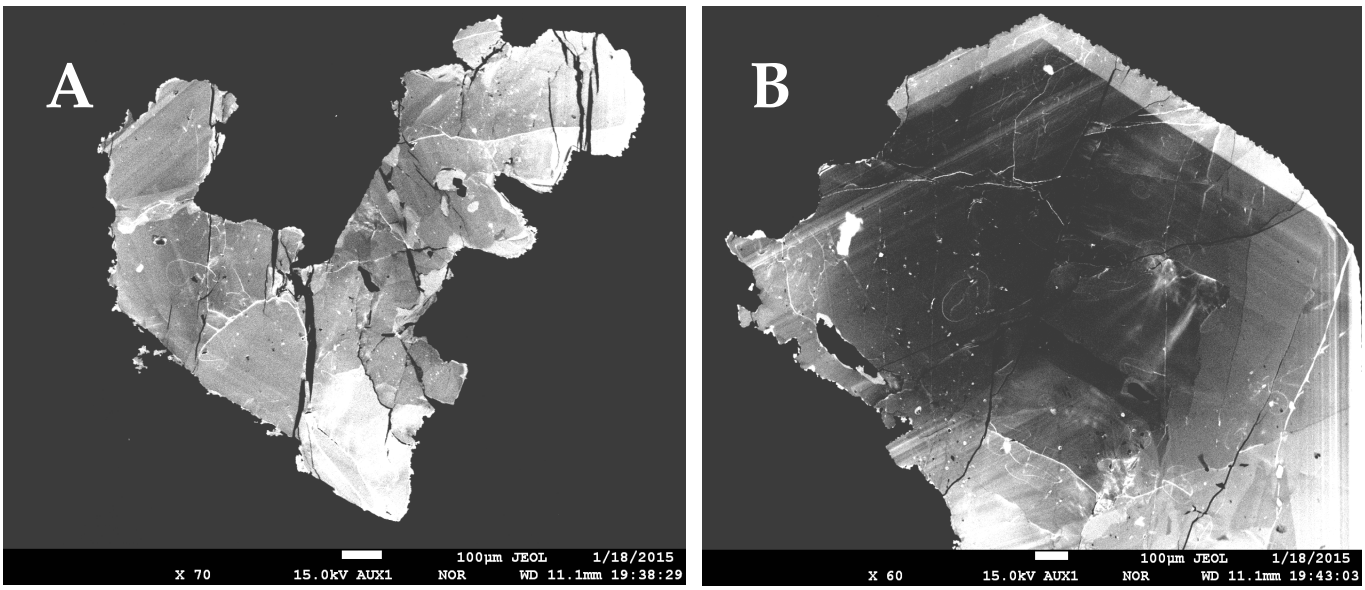

Figure 3. *Cont.*

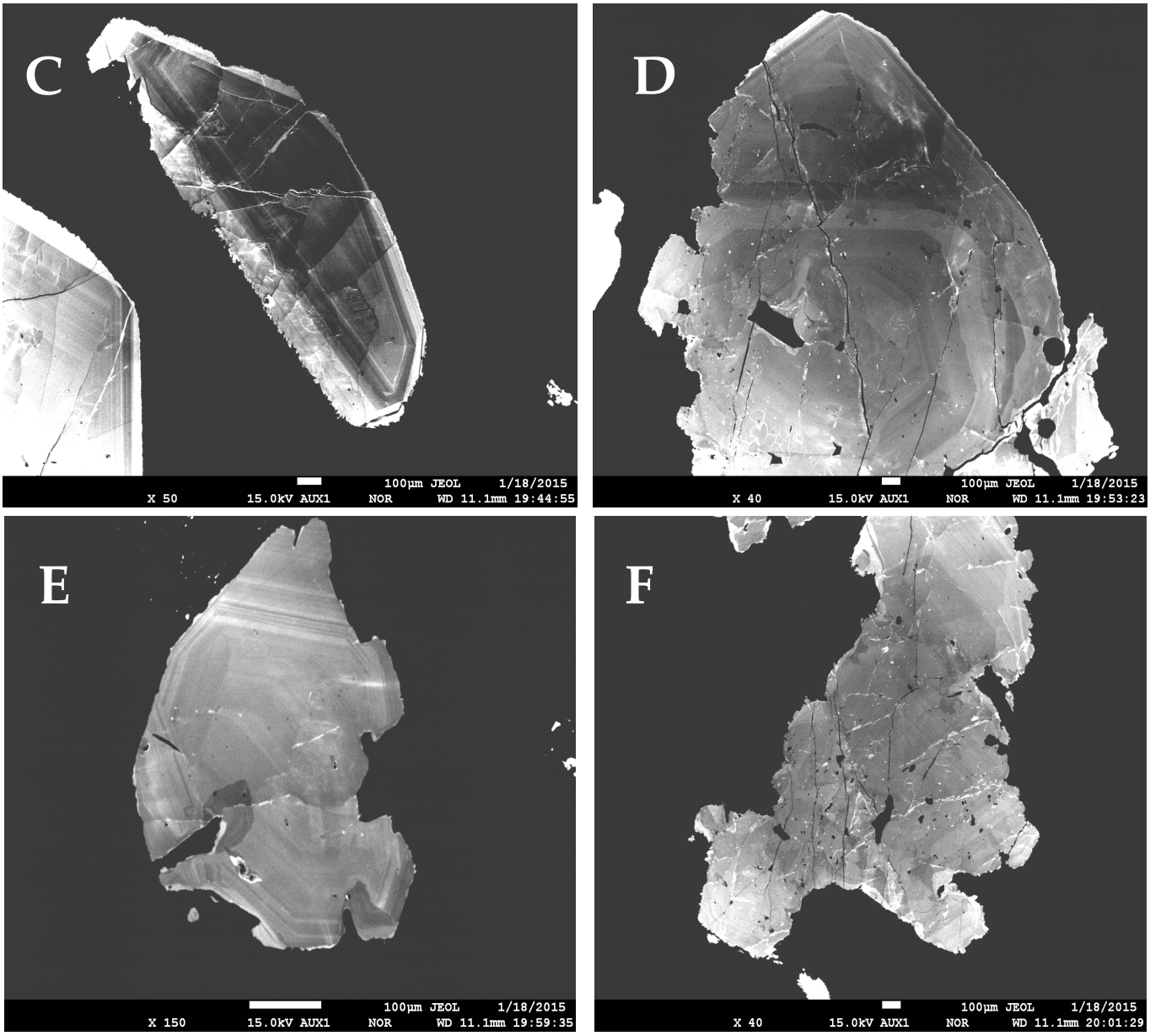

Figure 3. Cathodoluminescence images of scheelite from the analyzed skarns. (**A**) Internal structure of a scheelite grain as determined by CL, showing mainly irregular and diffuse zones. Sample 2506, Ciclova. (**B**,**C**) Oscillatory-zoned crystals with large regular dark CL zones (**B**) and late-stage overgrowth with lighter CL response (**B**,**C**). Sample 2569 Oravița. (**D**) Crystal of scheelite with diffuse CL zoning (center) with peripheral oscillatory zoning suggesting growth in tetrahedral symmetry. Note the recrystallized grains on the border with a light CL color. Sample 2536 Băița Bihor. (**E**) Oscillatory-zoned scheelite crystal, with peripheral regular (i.e., constant width), sharp, and distinct contacts. Sample 2544 Băița Bihor. (**F**) Homogenous CL-response scheelite grain (center) with peripheral irregular zones and lighter CL-response phases on fissures. Sample 2593 Băița Bihor.

5. Chemical Data

Electron-microprobe analyses of 30 representative scheelite crystals from Ciclova, Oravița, and Băița Bihor are given in Tables 2–4. The samples are indicated by numbers, whereas letters, when used, indicate different crystals in the same sample. Each analysis represents the average of N points of analysis across the same crystal from a thin section. Formulas were normalized on the basis of 4(O) atoms per formula unit (*apfu*), the resulting crystal-chemical formulas being, in all cases, definitory for terms close to the scheelite end-member of the scheelite-powellite solid solution series.

Table 2. Representative electron-microprobe analyses of scheelite from Ciclova *.

Sample	2506a	2506b	2506c	2509a	2509b	2509c	2534a	2534b	2575a	2575b	Mean
N (1)	12	15	16	11	13	13	14	11	12	11	128
WO_3	79.81	79.41	78.31	78.91	79.24	79.14	79.40	79.16	79.24	78.49	79.10
MoO_3	0.63	0.63	1.21	1.21	1.14	1.05	0.77	1.12	1.12	0.87	0.97
Bi_2O_3	0.03	0.02	0.03	0.01	0.04	0.02	0.01	0.03	0.03	0.04	0.03
CaO	19.44	19.40	19.45	19.49	19.38	19.37	19.31	19.31	19.32	19.25	19.37
MgO	0.00	0.02	0.00	0.00	0.00	0.00	0.00	0.00	0.00	0.00	0.00
MnO	0.02	0.03	0.04	0.03	0.02	0.03	0.06	0.04	0.03	0.02	0.03
FeO (2)	0.03	0.06	0.03	0.02	0.04	0.05	0.02	0.02	0.04	0.04	0.04
PbO	0.03	0.05	0.03	0.03	0.05	0.07	0.07	0.02	0.05	0.00	0.04
CuO	0.01	0.01	0.03	0.03	0.02	0.02	0.05	0.01	0.03	0.02	0.02
Total	100.00	99.63	99.13	99.73	99.93	99.75	99.67	99.71	99.86	98.73	99.60
Number of Cations on the Basis of 4(O)											
W	0.988	0.986	0.974	0.976	0.979	0.980	0.986	0.980	0.980	0.982	0.981
Mo	0.013	0.013	0.024	0.024	0.023	0.021	0.015	0.022	0.022	0.018	0.019
Bi	0.000	0.000	0.000	0.000	0.000	0.000	0.000	0.000	0.000	0.000	0.000
Ca	0.995	0.996	1.000	0.996	0.990	0.992	0.991	0.989	0.988	0.996	0.994
Mg	0.000	0.001	0.000	0.000	0.000	0.000	0.000	0.000	0.000	0.000	0.000
Mn	0.001	0.001	0.002	0.001	0.001	0.001	0.002	0.002	0.001	0.001	0.001
Fe^{2+}	0.001	0.002	0.001	0.001	0.002	0.002	0.001	0.001	0.002	0.002	0.002
Pb	0.000	0.001	0.000	0.000	0.001	0.001	0.001	0.000	0.001	0.000	0.001
Cu	0.000	0.000	0.001	0.001	0.001	0.001	0.002	0.000	0.001	0.001	0.001
Composition in End Members (mol.%)											
scheelite	98.70	98.70	97.60	97.60	97.70	97.90	98.50	97.80	97.80	98.20	98.10
powellite	1.30	1.30	2.40	2.40	2.30	2.10	1.50	2.20	2.20	1.80	1.90

* EMP analyses, results expressed in wt.%; (1) number of point analyses on the same crystal; (2) total iron taken as divalent.

Table 3. Representative electron-microprobe analyses of scheelite from Oravița *.

Sample	2537a	2537b	2537c	2538a	2538b	2538c	2539	2568	2569a	2569b	Mean
N (1)	5	6	7	9	7	6	11	16	12	11	90
WO_3	79.86	79.30	79.87	80.38	80.36	80.48	79.42	77.79	77.95	77.82	79.03
MoO_3	0.14	0.33	0.25	0.37	0.32	0.27	1.32	2.85	1.92	1.97	1.29
Bi_2O_3	0.01	0.01	0.00	0.01	0.01	0.00	0.02	0.02	0.00	0.01	0.01
CaO	19.29	19.53	19.55	19.42	19.36	19.44	19.56	19.90	19.46	19.42	19.53
MgO	0.00	0.01	0.01	0.00	0.01	0.01	0.01	0.01	0.00	0.00	0.01
MnO	0.00	0.00	0.01	0.00	0.00	0.00	0.00	0.00	0.01	0.01	0.00
FeO (2)	0.05	0.04	0.03	0.03	0.05	0.17	0.02	0.02	0.02	0.02	0.04
PbO	0.04	0.00	0.03	0.01	0.05	0.02	0.02	0.02	0.04	0.01	0.02
CuO	0.02	0.00	0.01	0.00	0.01	0.00	0.01	0.00	0.00	0.00	0.01
Total	99.41	99.22	99.76	100.22	100.17	100.39	100.38	100.61	99.40	99.26	99.94
Number of Cations on the Basis of 4(O)											
W	0.997	0.990	0.993	0.994	0.995	0.994	0.975	0.944	0.963	0.963	0.975
Mo	0.003	0.007	0.005	0.007	0.006	0.005	0.026	0.056	0.038	0.039	0.025
Bi	0.000	0.000	0.000	0.000	0.000	0.000	0.000	0.000	0.000	0.000	0.000
Ca	0.996	1.008	1.004	0.993	0.991	0.993	0.993	0.998	0.994	0.993	0.996
Mg	0.000	0.001	0.001	0.000	0.001	0.001	0.001	0.001	0.000	0.000	0.001
Mn	0.000	0.000	0.000	0.000	0.000	0.000	0.000	0.000	0.000	0.000	0.000
Fe^{2+}	0.002	0.002	0.001	0.001	0.002	0.007	0.001	0.001	0.001	0.001	0.002
Pb	0.001	0.000	0.000	0.000	0.001	0.000	0.000	0.000	0.001	0.000	0.001
Cu	0.001	0.000	0.000	0.000	0.000	0.000	0.000	0.000	0.000	0.000	0.000
Composition in End Members (mol.%)											
scheelite	99.70	99.30	99.50	99.30	99.40	99.50	97.40	94.40	96.20	96.11	97.50
powellite	0.30	0.70	0.50	0.70	0.60	0.50	2.60	5.60	3.80	3.89	2.50

* EMP analyses, results expressed in wt.%; (1) number of point analyses on the same crystal; (2) total iron taken as divalent.

Table 4. Representative electron-microprobe analyses of scheelite from Băița Bihor *.

Sample	2536	2544	2549	2552	2576	2577	2590	2591	2592	2593	Mean
N (1)	11	10	8	9	12	10	10	13	11	11	105
WO_3	79.70	79.48	79.56	78.41	78.81	78.93	78.60	79.28	79.49	78.97	79.13
MoO_3	0.63	0.73	0.61	1.13	1.29	0.88	1.16	1.17	0.84	0.88	0.95
Bi_2O_3	0.03	0.03	0.00	0.04	0.04	0.01	0.01	0.00	0.02	0.05	0.02
CaO	19.48	19.4	19.37	19.42	19.36	19.26	19.43	19.5	19.26	19.23	19.37
MgO	0.00	0.00	0.05	0.00	0.00	0.00	0.00	0.00	0.00	0.00	0.00
MnO	0.02	0.07	0.01	0.04	0.03	0.02	0.03	0.02	0.01	0.03	0.03
FeO (2)	0.04	0.03	0.09	0.03	0.07	0.03	0.01	0.03	0.04	0.03	0.04
PbO	0.04	0.02	0.08	0.03	0.04	0.01	0.03	0.05	0.04	0.00	0.03
CuO	0.01	0.00	0.01	0.02	0.03	0.03	0.03	0.03	0.03	0.01	0.02
Total	99.95	99.76	99.78	99.12	99.67	99.17	99.30	100.08	99.73	99.20	99.59
Number of Cations on the Basis of 4(O)											
W	0.987	0.986	0.987	0.976	0.975	0.984	0.976	0.978	0.986	0.984	0.982
Mo	0.013	0.015	0.012	0.023	0.026	0.018	0.023	0.023	0.017	0.018	0.019
Bi	0.000	0.000	0.000	0.000	0.000	0.000	0.000	0.000	0.000	0.001	0.000
Ca	0.997	0.995	0.993	0.999	0.991	0.992	0.998	0.994	0.988	0.991	0.994
Mg	0.000	0.000	0.004	0.000	0.000	0.000	0.000	0.000	0.000	0.000	0.000
Mn	0.001	0.003	0.000	0.002	0.001	0.001	0.001	0.001	0.000	0.001	0.001
Fe^{2+}	0.002	0.001	0.004	0.001	0.003	0.001	0.000	0.001	0.002	0.001	0.002
Pb	0.001	0.000	0.001	0.000	0.001	0.000	0.000	0.001	0.001	0.000	0.001
Cu	0.000	0.000	0.000	0.001	0.001	0.001	0.001	0.001	0.001	0.000	0.001
Composition in End Members (mol.%)											
scheelite	98.70	98.50	98.80	97.70	97.40	98.20	97.70	97.70	98.31	98.20	98.10
powellite	1.30	1.50	1.20	2.30	2.60	1.80	2.30	2.30	1.69	1.80	1.90

* EMP analyses, results expressed in wt.%; (1) number of point analyses on the same crystal; (2) total iron taken as divalent.

A few remarks must be drawn based on the results in Tables 2–4, as follows:

1. No obvious chemical zoning was observed at the level of individual crystals, in spite of the CL zoning described below. Qualitative elemental X-ray maps exemplified in Figure 4a,b don't show any zoning.
2. A slight overcompensation in the four-fold coordinated cations (i.e., W + Mo > 1) could be observed in some samples, particularly at Oravița (Table 3). This phenomenon was already observed in some other cases (e.g., [12,42,43]) and is probably due to the EMPA interference effect of tungstite (ideally $WO_3 \cdot H_2O$) or rather hydrotungstite (ideally $H_2WO_4 \cdot H_2O$), whose presence in all three occurrences was already mentioned [44].
3. The isomorphism in the scheelite–powellite solid solution series is very restricted, reaching up to 2.4 mol.% powellite at Ciclova, up to 5.6 mol.% at Oravița, and up to 2.6 mol.% at Băița Bihor. The X-ray elemental maps failed to identify a chemical zoning at the crystal level, in spite of the general opinion that the dark CL oscillatory bands described above are enriched in Mo (i.e., [45,46]).
4. Ba was sought but not detected, so the isomorphism toward ronpetersonite can't be considered.
5. The contents of stolzite (ideally $PbWO_4$) in the solid solution are insignificant, reaching up to 0.1 mol.%.
6. The small contents of Cu recorded in part of the samples could be rather due to submicrometer-sized cuprotungstite—ideally $Cu_2(WO_4)(OH)_2$—inclusions, probably intruded on the cleavage directions; these inclusions are too small to be seized by the X-ray imaging.

7. The collection of qualitative elemental X-ray maps (Figure 4a,b) together with SEM-EDS analyses confirmed that Sb and Bi are present in minor amounts in some scheelite grains. Apparently, both trivalent Sb and Bi are substitutes for Ca^{2+} through a mechanism similar to those reported by [47] and referred to in the case of REE and Y, i.e., $2Bi^{3+}(Sb^{3+}) + \square\ Ca = 3Ca^{2+}$, where $\square$ Ca represents a vacancy site.

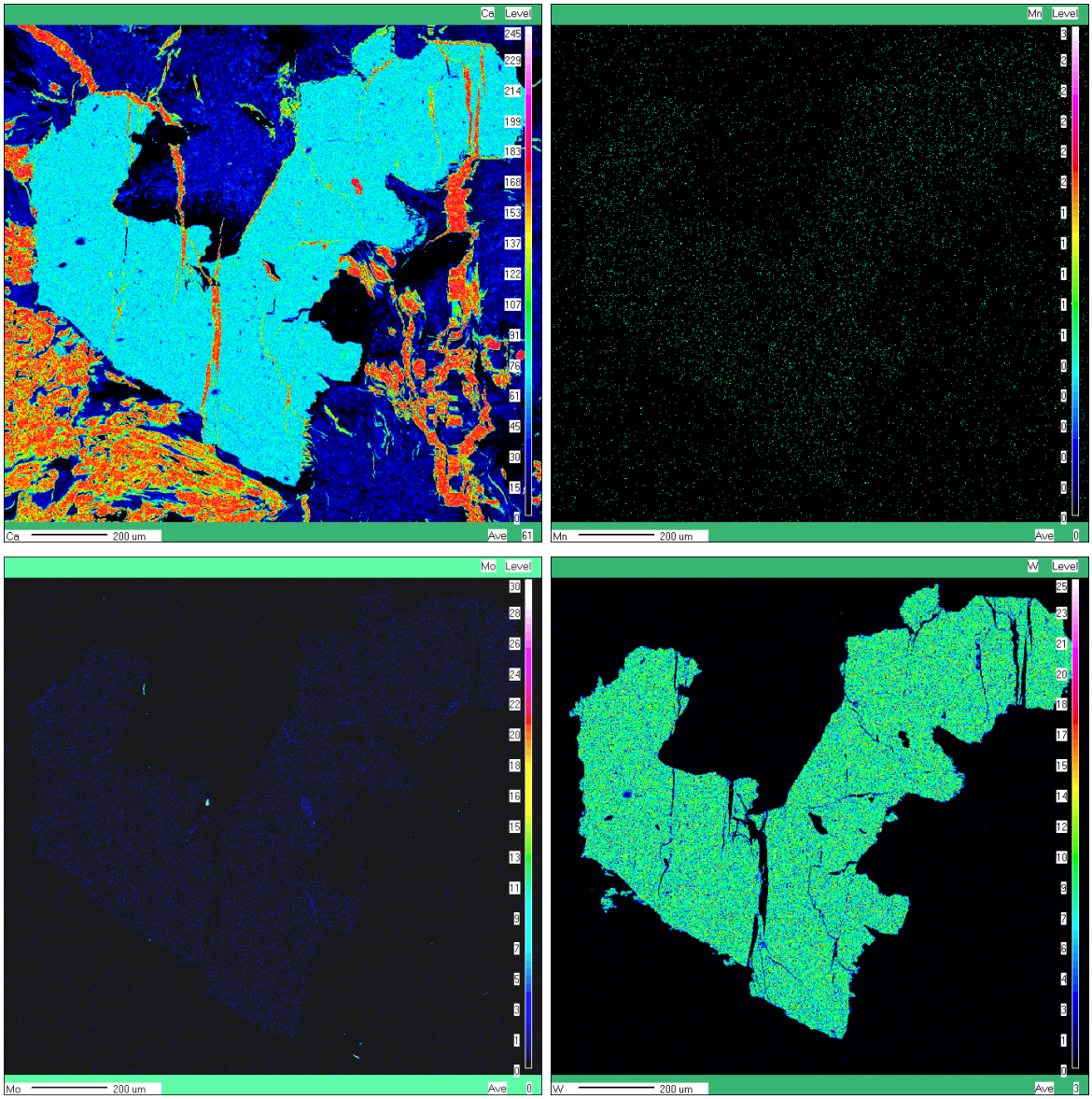

Figure 4. *Cont.*

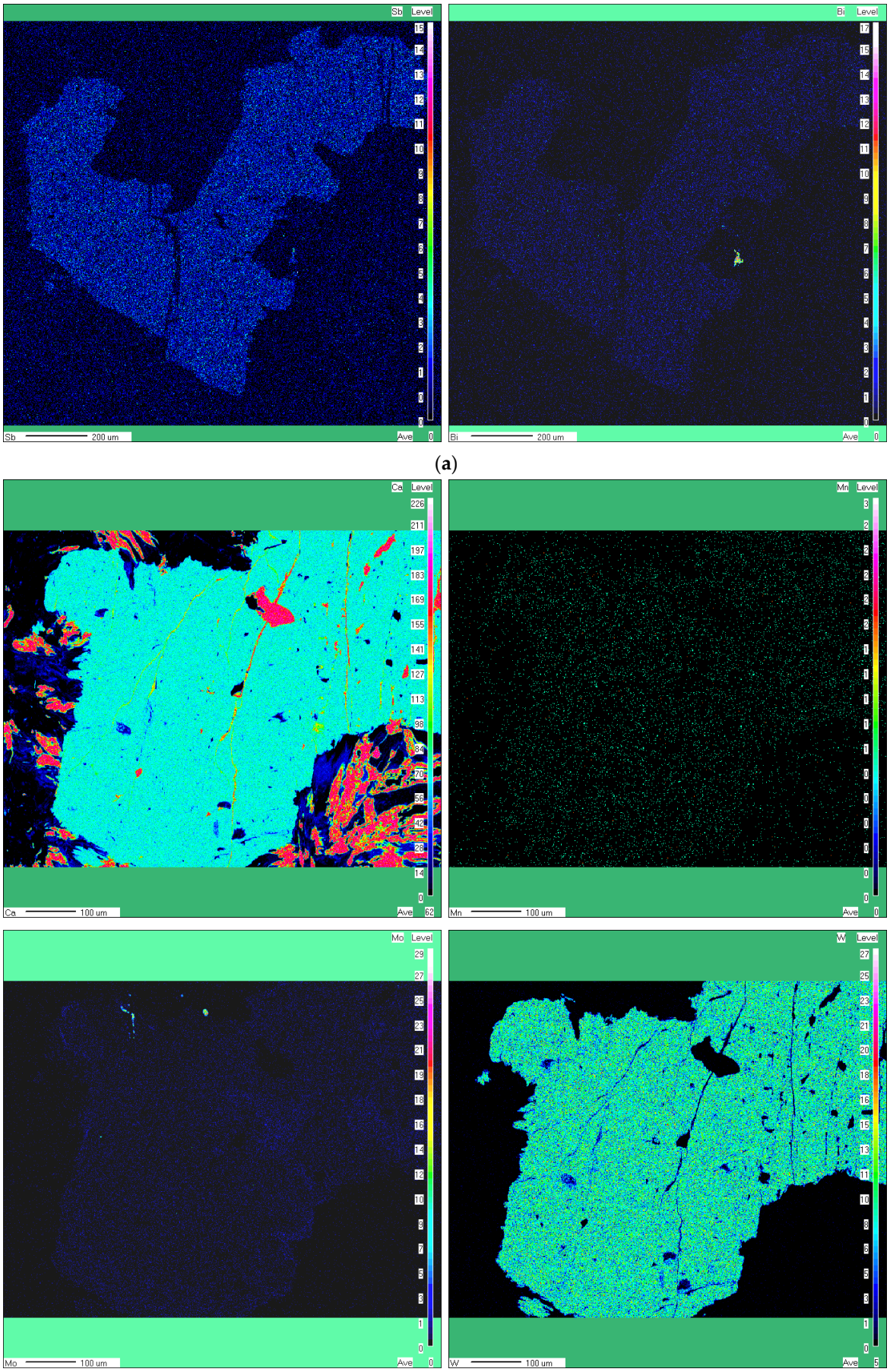

(**a**)

Figure 4. *Cont*.

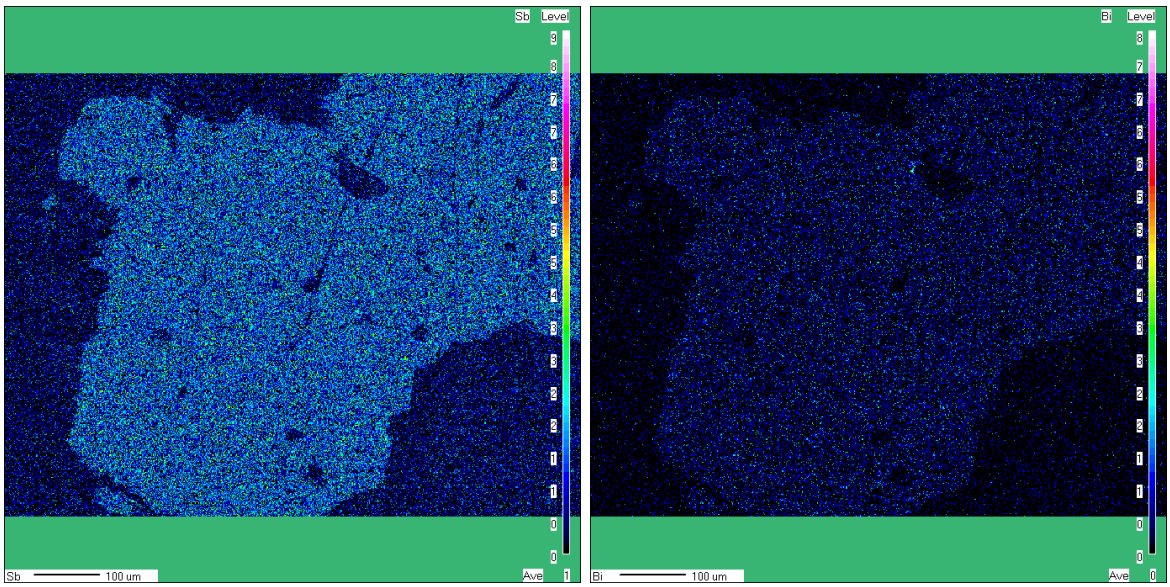

(**b**)

Figure 4. (**a**) Elemental X-ray maps showing the spatial distribution of Ca, Mn, Mo, W, Sb, Bi in a selected crystal of scheelite from Ciclova (Sample 2506). (**b**) Elemental X-ray maps showing the spatial distribution of Ca, Mn, Mo, W, Sb, Bi in a selected crystal of scheelite from Băița Bihor (Sample 2593).

6. X-Ray Powder Diffraction Data

Cell parameters of 5 representative samples of scheelite were successfully refined by least squares, based on a tetragonal $I4_1/a$ cell (e.g., [48]). The patterns were indexed on the basis of Miller indices obtained by structural refinement that closely correspond to PDF 41-1431 [49]. Three XRD powder patterns given for scheelite samples from Băița Bihor by [16] and three others given for scheelite samples from Oravița–Ciclova and Băița Bihor by [44] were also used for calculation of cell parameters. The results are given in Table 5, together with 4 sets of cell parameters obtained by single-crystal X-ray refinement.

Table 5. Cell parameters of selected samples of scheelite from the analyzed skarn occurrences.

Sample	*a* (Å)	*c* (Å)	*V* (Å^3)
	Ciclova		
1189 [(1)]	5.230(2)	11.356(7)	310.67(8)
2492 [(2)]	5.2431(1)	11.3743(5)	312.68(2)
2506	5.243(4)	11.366(14)	312.46(53)
2509	5.234(2)	11.393 (15)	312.06(37)
	Oravița		
535 [(1)]	5.231(1)	11.343(3)	310.41(14)
2491	5.239(4)	11.402 (9)	313.02(53)
2537	5.229(4)	11.372(14)	310.92(57)
2569 [(2)]	5.2425(2)	11.3703(7)	312.499(2)
	Băița Bihor		
Sch 01 [(3)]	5.240(2)	11.373(5)	312.25(20)
Sch 02 [(3)]	5.2384(9)	11.370(4)	312.00(12)
Sch 03 [(3)]	5.2377(8)	11.366(2)	311.82(10)
1050 [(1)]	5.232(2)	11.375(8)	311.34(25)
2536	5.243(1)	11.380(4)	312.85(16)
2576 [(2)]	5.2409(2)	11.3705(6)	312.314(2)
2593 [(2)]	5.2388(2)	11.3667(9)	311.959(1)

[(1)]—calculated after the XRD powder patterns given by [44]. [(2)]—data obtained by single-crystal refinement. [(3)]—calculated after the XRD powder patterns given by [16].

The cell parameters in Table 5 are generally close to the cell parameters reported by various authors for stoichiometric scheelite {i.e., a = 5.24294(6) Å and c = 11.373(7) Å according to [49]; a = 5.2419(5) Å and c = 11.376(1) Å according to [50]; and a = 5.23643(5) Å and c = 11.33815(33) Å according to [51]} and also to similar values reported for scheelite samples close to stoichiometry: e.g., [43,52]. The low content of powellite in the solid solution series of the analyzed scheelite samples is quite evident since powellite has lower a and higher c cell parameters {e.g., a = 5.2256(5) Å and c = 11.434(1) Å according to [50], a = 5.222(1) Å and c = 11.425(3) Å according to [52], or a = 5.220(2) Å and c = 11.407(10) Å according to [53]}.

7. Physical Properties

Macroscopically, scheelite from all three occurrences occurs as translucent, turbid-white to yellow crystals. A glassy luster can be observed on the distinct cleavage on {101}, whereas the normal luster is waxy vitreous. The mineral is nonfluorescent in long-wave UV light (366 nm) and shows generally strong blue fluorescence in short-wave UV light (254 nm). Exceptions occur at some samples from Oravița, where a yellow tint of fluorescence also occurs. The usual fluorescence tints are better depicted in Figures 2 and 5 and indicate low contents of powellite in the solid-solution series [54].

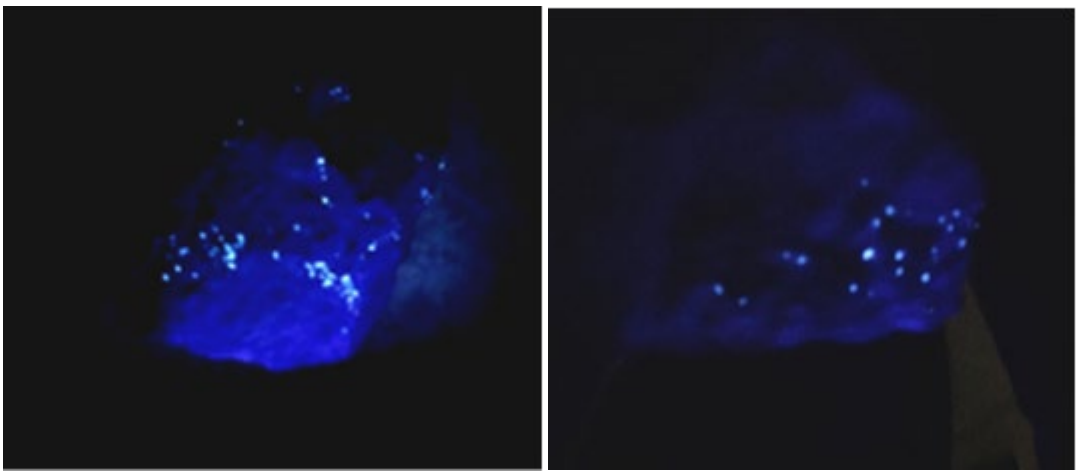

Figure 5. UV photographs of representative scheelite-bearing samples. (**Left**) Scheelite in a quartz-pyrite-chalcopyrite veinlet from Ciclova (Lobkowitz–Sample 2506). The biggest crystal is 12 mm across. (**Right**) Scheelite disseminated in a diopside–phlogopite skarn from Băiţa Bihor (Baia Roşie–Sample 2544). The biggest crystal is 15 mm across.

Compared with the standard color card proposed by [54], the scheelite samples from Ciclova, Băița Bihor, and the large majority of those from Oravița may contain up to 3 mol.% powellite in solid solutions, whereas the yellow-tinted scheelite from Oravița contains up to 6 mol.% powellite, which perfectly agrees with data in Tables 2–4. Scheelite samples from Băița Bihor seem to correspond to the scheelite III type described by [16] based on fluorescence colors.

Under the electron beam, scheelite samples show a strong cathodoluminescence (CL) response of light blue color, which can be due to the self-activated emission band (also referred to as a self-luminescence band, SB), which produces a broad spectral peak that is intrinsic to the mineral, this being attributed to the $(WO_4)^{2-}$ tetrahedral complex ([45] and referred works). A cathodoluminescence zoning of the individual crystals, described in many worldwide occurrences (e.g., [42,45–47,55,56]), can be observed in all the analyzed samples and is illustrated in Figure 3. The subhedral scheelite grains display in many cases oscillatory CL zones characterized by alternating dark and bright CL bands

with sharp boundaries, similar to Type 1 scheelite described by [46] or S-type described by [55]. Crystals of scheelite could also display bright peripheral CL concentric zones with central homogenous dark CL zones, suggesting the optical lamellar zoning of garnet and resembling Type 2 scheelite described by [46]: Figure 3.

Optically, the mineral is uniaxial positive. The indices of refraction of three representative samples (one for each occurrence), taken as the average of five measured values on 5 different crystals from the same sample, are given in Table 6. The indices of refraction in Table 6 are in the range of the higher values reported by [57] for scheelite, i.e., $\omega = 1.911 - 1.934$ and $\varepsilon = 1.926 - 1.953$. As the refraction indices presumably decrease with increasing content of Mo [57], the values in Table 6 are indicative of terms with low contents of powellite in the solid solution series. The mean refraction index, calculated as $n = (2\omega + \varepsilon)/3$ [58], is also given in Table 6.

Table 6. Physical constants of hydrothermal scheelite from the analyzed skarns.

Sample	**2509b**	**2539**	**2544**
Occurrence	Ciclova	Oraviţa	Băiţa Bihor
ω	1.928	1.929	1.931
ε	1.945	1.946	1.948
n	1.934	1.935	1.937
M_{mol} [(1)]	286.298	285.614	286.801
V (Å^3)	313.11	311.90	312.31
D_m (g/cm^3)	6.08(1)	6.08(1)	6.10(1)
D_x (g/cm^3)	6.071	6.080	6.098
K_P [(2)]	0.1536	0.1538	0.1536
K_C	0.1492	0.1494	0.1488
$1 - K_P/K_C$	−0.0298	−0.0294	−0.0323
K_P ′[(3)]	0.1538	0.1538	0.1537
$1 - K_P'/K_C$	−0.0313	−0.0293	−0.0327

[(1)] Molecular mass in atomic mass units; [(2)] based on measured density (D_m); [(3)] based on calculated density (D_x).

The D_x calculated densities of three representative samples (one for each occurrence) were obtained on the basis of chemical data in Tables 2–4 and of unit cell volumes in Table 6, for Z = 4 formula units per cell [59]. The values obtained are given in Table 6. The mean measured density D_m, taken as the average of measurements on 10 different grains, is also included in Table 6 and compares well with the calculated densities. Both values, as well as the mean refraction indices, were used to calculate the physical refractive energy as $K_P = (n - 1)/D$.

The chemical refractive energy (K_C) values in Table 6 are based on the oxide content issued from EMP analyses of the three samples and on the constants for oxides given by [58,60], excepting that for WO_3, taken from [61], i.e., k (WO_3) = 0.133.

The calculation of the Gladstone-Dale compatibility index ($1 - Kp/Kc$) yielded the values given in Table 6, indicative of excellent agreement between physical and chemical data [60]. The use of a Gladstone-Dale constant for WO_3 as indicated by [58,60], i.e., k (WO_3) = 0.152 or k (WO_3) = 0.171, respectively, results in poor compatibilities.

8. Structure

The atomic structure of scheelite was refined by both neutron diffraction [48] and single-crystal X-ray diffraction ([52,59]). The results are coincident in describing a structure consisting of two intercalated polyhedral lattices, one composed of slightly deformed WO_4 tetrahedra and another by CaO_8 dodecahedra (bidisphenoids) described by eight-fold coordinated Ca cations. The structure features a tetragonal unit cell with space group

$I4_1/a$ (Z = 4), which was confirmed during this study. As the powellite contents in the analysed samples are low, the eventual Mo atoms were not included in the refinement of the X-ray data.

Details of the scheelite structure obtained during this work are shown in Figure 6.

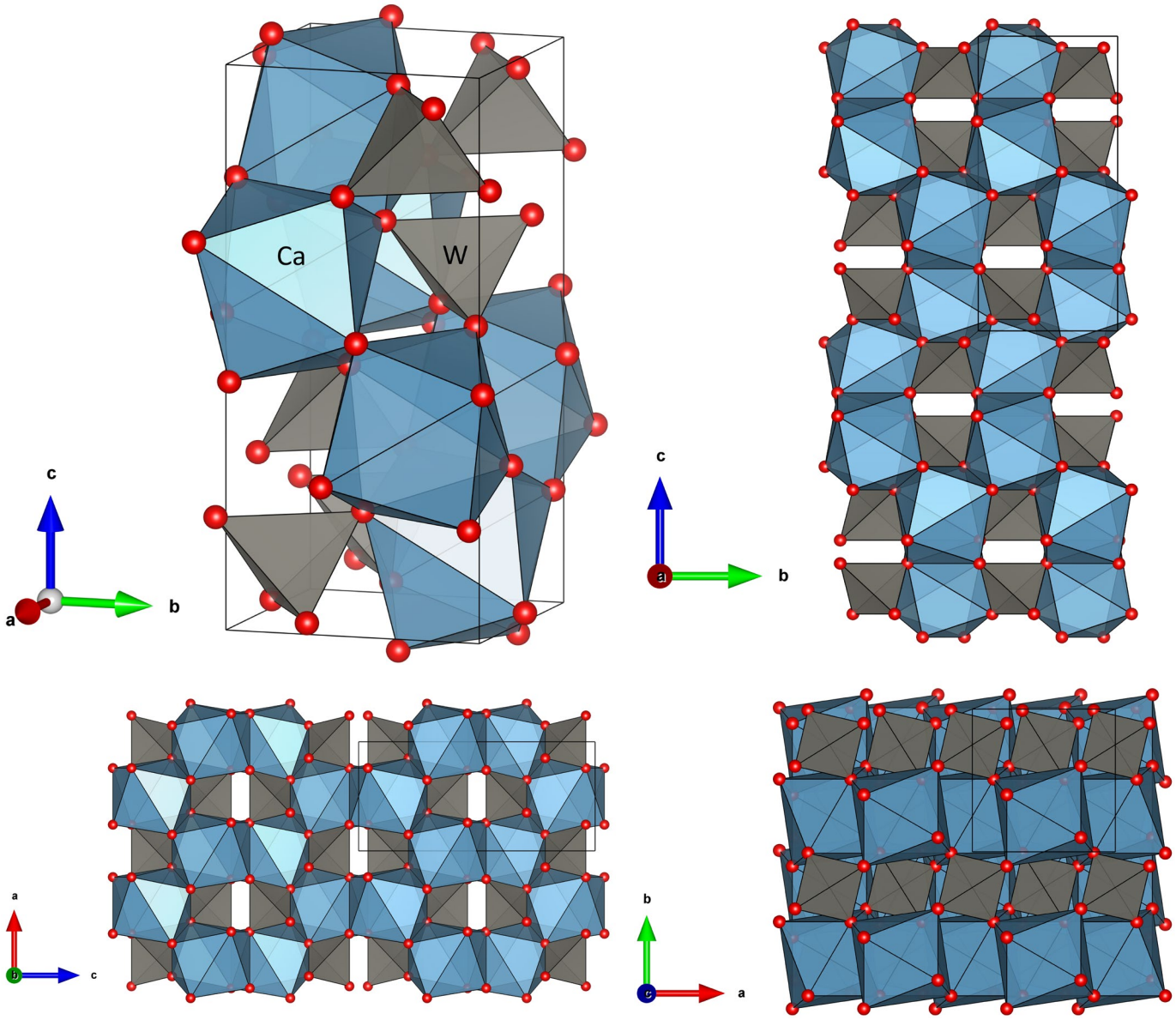

Figure 6. Projections of the structure of scheelite along the *c*-axis, showing the structural polyhedra. The grey tetrahedra represent WO_4, the gray-blue polyhedra represent CaO_8 dodecahedra, and the red balls represent O^{2-} corners. (**Top**): projection of the structure on (100), at the level of unit-cell (**left**), and at the level of the formula unit (**right**). (**Bottom**): projection of the structure at the level of the formula unit on (010)—(**left**) and (001), respectively (**right**).

Table 7 depicts the data collection and structure refinement details for the analyzed samples, whereas positional and displacement parameters are given in Tables 8–11. The corresponding *.cif files are given as Supplementary Materials.

Table 7. Data collection and structure refinement details for Romanian scheelite.

Sample **Occurrence**	**2509** **Ciclova**	**2538** **Oravița**	**2544** **Băița Bihor**
a (Å)	5.2459(10)	5.2380(2)	5.2409(2)
c (Å)	11.3777(5)	11.3679(8)	11.3705(6)
V (Å^3)	313.108(18)	311.90(3)	312.31(3)
Z	4	4	4
D_x (g/cm^3)	6.108	6.132	6.124
Crystal size (mm^3)	0.177 × 0.124 × 0.091	0.35 × 0.22 × 0.1	0.283 × 0.21 × 0.195
Absorption coefficient (mm^{-1})	38.351	38.502	38.449
F(000)	504	504	504
Max. 2ϴ (°)	56.994	57.766	57.74
Range of indices	$-6 \leq h \leq 6$ $-5 \leq k \leq 6$ $-13 \leq l \leq 15$	$-5 \leq h \leq 6$ $-4 \leq k \leq 6$ $-14 \leq l \leq 14$	$-7 \leq h \leq 6$ $-7 \leq k \leq 5$ $-12 \leq l \leq 15$
Number of measured reflections	1031	1011	1051
Number of unique reflections	188	191	194
Independent non-zero reflections	176	180	180
Criterion for observed reflections	$I > 2\sigma(I)$	$I > 2\sigma(I)$	$I > 2\sigma(I)$
Number of refined parameters	16	16	16
R int	0.0212	0.0261	0.0327
R sigma	0.0158	0.0181	0.0216
R_1 (F) with $F_0 > 4\ \sigma(F_0)$ *	0.0144	0.0189	0.0216
R_1 (F) for all the unique reflections *	0.0165	0.0204	0.0237
wR_2 (F_2) *	0.0348	0.0477	0.0539
S ("goodness of fit")	1.227	1.267	1.206
Min./max. residual e density, (eÅ^{-3})	−0.88/0.61	−2.46/0.77	−1.71/1.00
Weighing scheme		$1/(\sigma^2(I)^2 + 0.0025(I)^2$	

* Notes: $R_1 = \Sigma(|Fobs| - |Fcalc|)/\Sigma|Fobs|$; $wR_2 = \{\Sigma[w(F^2obs - F^2calc)^2]/\Sigma[w(F^2obs)^2]\}^{1/2}$. $W = 1/[s^2(F_0^2) + (aP)^2 + bP]$, where $P = [2F_c^2 + Max(F_0^2,0)]/3$, where a, b are shown in the refinement process.

Table 8. Anisotropic displacement parameters (Å^2) for scheelite.

Atom	U_{11}	U_{22}	U_{33}	U_{23}	U_{13}	U_{12}
Sample 2509 Ciclova						
Ca	3.4(9)	3.4(9)	1.8(11)	0	0	0
W	3.96(17)	3.96(17)	4.9(2)	0	0	0
O	14.0(19)	14.7(18)	12.0(15)	−2.0(14)	−1.1(13)	−2.7(14)
Sample 2538 Oravița						
Ca	2.2(12)	2.2(12)	2.8(15)	0	0	0
W	2.6(2)	2.6(2)	6.2(3)	0	0	0
O	11(2)	11(2)	10(2)	1.9(17)	−2.0(17)	0.3(15)
Sample 2544 Băița Bihor						
Ca	7.7(13)	7.7(13)	4.2(16)	0	0	0
W	7.6(3)	7.6(3)	8.4(3)	0	0	0
O	16(2)	18(2)	15(2)	−1(2)	−3(2)	1.9(18)

Table 9. Atom coordinates and isotropic displacement parameters (Å^2) for scheelite.

Atom	*x*	*y*	*z*	*U* (eq)
Sample 2509 Ciclova				
Ca	0	7500	8750	2.9(8)
W	0	2500	6250	4.27(15)
O	1515(6)	4909(6)	7108(3)	13.6(10)
Sample 2538 Oravița				
Ca	0	7500	3750	2.4(10)
W	5000	7500	6250	3.8(2)
O	2594(7)	5980(7)	5392(4)	10.7(12)
Sample 2544 Băița Bihor				
Ca	0	7500	3750	6.5(11)
W	5000	7500	6250	7.8(2)
O	2592(9)	6000(8)	5393(4)	16.4(14)

Table 10. Bond distances (Å) and occupancies observed in the crystal structure of scheelite.

Sample	2509	2538	2544
Occurrence	Ciclova	Oravița	Băița Bihor
Bond distances (Å)			
Ca-O x 4	2.443(4)	2.442(5)	2.440(5)
Ca-O x 4	2.478(4)	2.474(4)	2.482(5)
W-O x 4	1.784(4)	1.781(4)	1.778(5)
Occupancy			
Ca	0.83(15)	0.84(2)	0.83(2)
W	0.91(10)	0.91(14)	0.87(15)

Table 11. Detailed bond-valence table (v_u) for the crystal structure of scheelite *.

	Sample 2509 Ciclova			Sample 2538 Oravița			Sample 2544 Băița Bihor		
	Ca	W	Σ	Ca	W	Σ	Ca	W	Σ
O	0.276 × 4 ↓ 0.251 × 4 ↓	1.436 × 4 ↓	1.963	0.277 × 4 ↓ 0.254 × 4 ↓	1.444 × 4 ↓	1.98	0.278 × 4 ↓ 0.249 × 4 ↓	1.456 × 4 ↓	1.98
Σ	2.11	5.73		2.12	5.77		2.11	5.82	

* bond-valence parameters adjusted after [62].

The structure can be visualized as an assembly of CaO_8 dodecahedra and WO_4 tetrahedra. Each CaO_8 dodecahedron is connected to four other dodecahedra through edge-sharing, resulting in zigzag chains that develop along the c axis. WO_4 tetrahedra are isolated from each other and connected to CaO_8 dodecahedra via bridging oxygen atoms; each oxygen atom is connected to two Ca atoms and one W atom. CaO_8 dodecahedra are described by two distinct Ca−O distances (e.g., Table 11) and eight distinct O−Ca−O angles, while WO_4 tetrahedra could be fairly described by a single W−O distance and two distinct O−W−O angles. In fact, the isolated WO_4 tetrahedron is compressed along the c axis by 7% over a regular tetrahedron [51], which is better depicted by data in Table 10. Note that the site occupancies observed in Table 10 suggest mixed occupancies in both Ca and W sites and the non-stoichiometry of the analyzed samples with site populations involving substitutions in both structural sites, as given in Chapter 5.

9. Infrared and Raman Behavior

The infrared and Raman spectra recorded for representative scheelite samples from Ciclova, Oravița, and Băița Bihor are shown in Figures 7 and 8, respectively. An attempt to assign the vibrational bands in the Raman and infrared spectra to specific vibrational modes, together with the character and relative intensities of the bands in the infrared spectra, is included in Table 12.

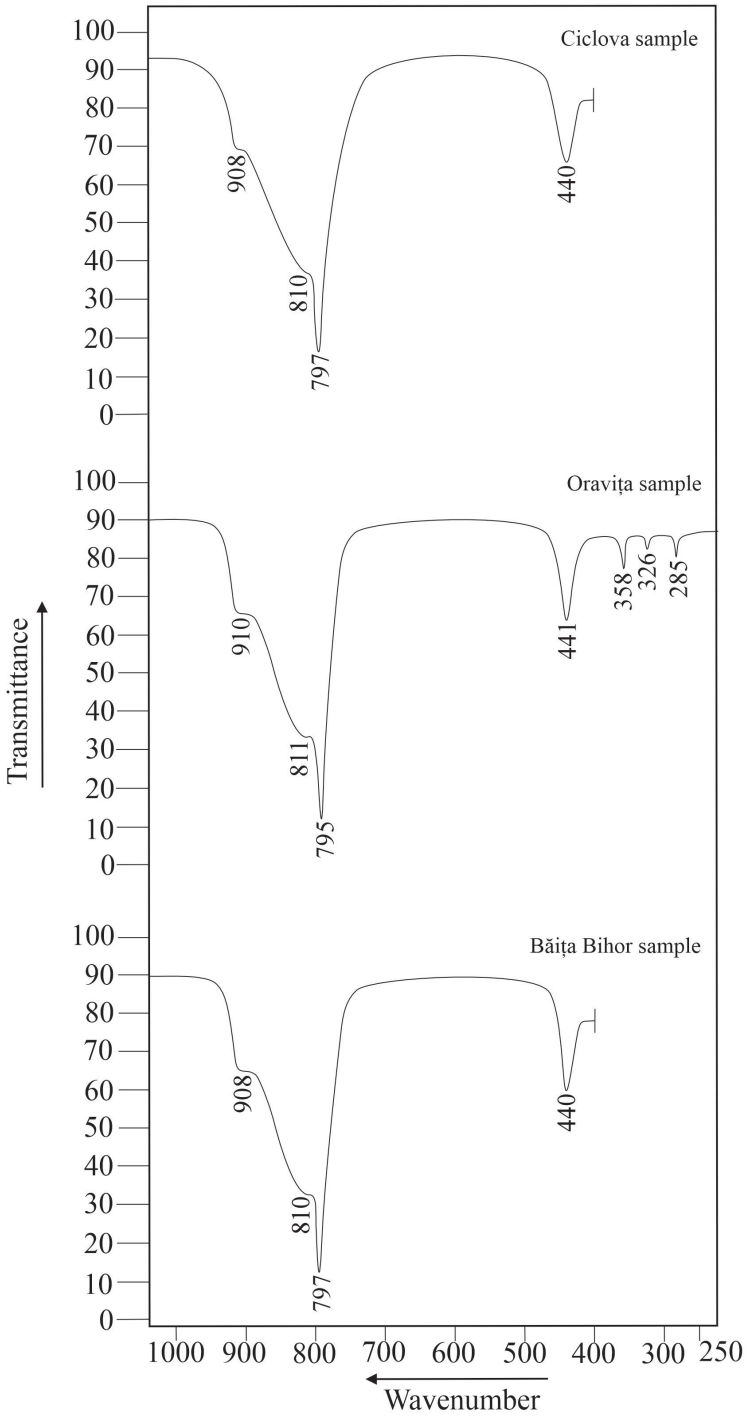

Figure 7. FTIR (**top**, **bottom**) and IR (**middle**) spectra of scheelite samples from Romanian skarns. From top to bottom: Sample 2509 Ciclova (**top**), sample 535 Oravița (**middle**), and sample 2544 Băița Bihor.

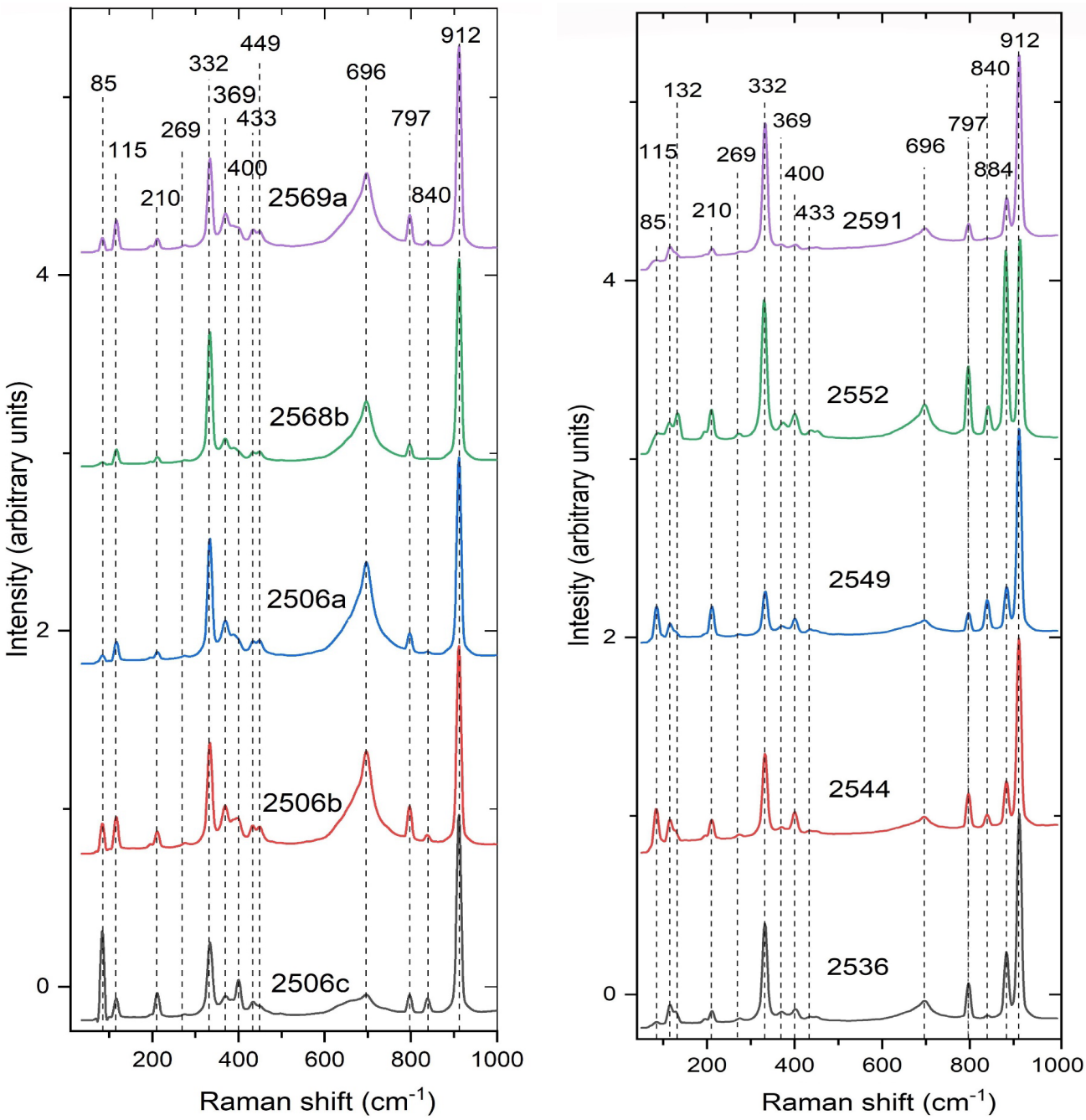

Figure 8. Raman spectra of selected samples of scheelite from Oravița (Samples 2569 a, 2568 b), Ciclova (Samples 2506 a, b, c), and Băița Bihor (Samples 2536, 2544, 2549, 2552, and 2591). Records were made aleatory, on different crystal faces.

Assigning vibrational bands in the Raman and infrared spectra to specific vibrational modes was considerably facilitated by the structure determinations, as well as by previous works of [11,12,63–71] for infrared spectra and of [11,65,70,72–78] for the Raman behavior.

IR spectra in Figure 7 show, at first view, the deviation of the main vibrational bands assignable to the WO_4 structural groups from the values given by [79] for the WO_4 tetrahedra with ideal T_d symmetry (i.e., ν_1 = 931 cm^{-1}, ν_3 = 833 cm^{-1}, ν_2 = 373 cm^{-1} and ν_4 = 320 cm^{-1}), as well as a superior band multiplicity. Note that, in scheelite, the ν_2 out-of-plane bending occurs at higher wavenumbers than the ν_4 in-plane bending, representing an opposite relation to the usual order. This relation, which implies that $\nu_2 > \nu_4$, was proven, based on force field studies, by [68]. Band assumptions in Table 12 were made consequently. Excepting the ν_1 symmetric stretching, vibrational modes of the $[WO_4]^{2-}$ group (i.e., the

ν_3 antisymmetric stretching and the two bending modes) are double degenerate. The band assignable to the ν_1 symmetric stretching, predicted by [68] to occur at 903 cm^{-1}, is materialized by a shoulder on the complex of bands at 750–900 cm^{-1}, which materializes the ν_3 antisymmetric stretching vibration of the WO_4 group (simply degenerate according to [67], and double degenerate according to [11,65,68,70]. The four bands found by [12] in the same region are certainly due to admixed secondary tungstates or, more probably, to the presence of two generations of scheelite, with different powellite contents. The ν_2 out-of-plane bending vibration of the $[WO_4]^{2-}$ group was found in the range of 428–441 cm^{-1}: [11,12,65–67,71]. Accepting that the two shoulders of the broad complex of bands centered at ~ 810 cm^{-1} materializes the ν_1 symmetric stretching (shoulder at higher frequency) and the ν'_3 antisymmetric stretching (shoulder at lower frequency) of the $[WO_4]^{2-}$ group, respectively, and that the band recorded at 286 cm^{-1} in the infrared spectrum in Figure 7 materializes in reality the ν'_4 in-plane bending [67], the multiplicity of bands in the infrared absorption spectrum ($1\nu_1 + 2\nu_3 + 2\nu_2 + 2\nu_4$) is consistent with the S_4 punctual symmetry of the tungstate anion, agreeing with the structural data. This point group symmetry was also deduced by [73,76,80] on the basis of the multiplicity of the Raman bands. Comparative studies on the IR behavior of $CaWO_4$ vs. $CaMoO_4$ (e.g., [65,67]) failed to prove any dependence of the positions of the main bands in the IR spectra on the Mo-for-W substitution. The slight differences in the position of the IR bands in our spectra do not consequently depend on the different powellite contents in the solid solution series of the analyzed samples.

Table 12. Positions and assignments of the FTIR and Raman bands recorded for scheelite from Romanian occurrences [(1)].

Structural Group	Vibrational Mode	Wavenumber (cm^{-1})								Character, Intensity [(4)]
		Calculated		Ciclova		Oravița		Băița Bihor		
		IR [(2)]	Raman [(3)]	FTIR	Raman	IR	Raman	FTIR	Raman	
WO_4	ν_1 (A_g) symmetric stretching	903	912	908	911	910	911	908	913	shd, s
WO_4 (?)	ν'_1 (B_g) (?)	-	893	-	-	-	-	-	883	-
WO_4	ν_3 (B_g) antisymmetric stretching	808	838	810	838	811	839	810	841	sh, vs
WO_4	ν'_3 (E_g) antisymmetric stretching	795	780	797	797	795	797	797	797	shd, s
WO_4	ν_2 (A_g) out-of-plane bending	418	439	440	434	441	434	440	437	sh, m
WO_4	ν'_2 ($E_g + B_g$) out-of-plane bending	-	403	-	401	-	400	-	402	-
WO_4	ν_4 (B_g) in-plane bending	359	-	-	369	358	369	-	370	sh, w
WO_4	ν'_4 (E_g) in-plane bending	348	330	-	333	326	333	-	332	sh, m
WO_4	rotation R$\parallel$ (A_g)	286	280	-	275	285	-	-	274	sh, w
WO_4	rotation R$\perp$ (E_g)	-	207	-	211	-	211	-	210	
CaO_8, WO_4	translation (E_g) Ca/Ca	-	196	-	193	-	193	-	193	
CaO_8, WO_4	translation (B_g) W/W	-	115	-	116	-	116	-	115	
CaO_8, WO_4	translation ($E_g + B_g$) W/W	-	83	-	84	-	84	-	85	

[(1)] Assumptions according to the authors referred to in the text; [(2)] after [68]; [(3)] after [70,80]; [(4)] character of the bands on IR (FTIR) spectra: s = strong; m = medium; w = weak; vs = very strong; sh = sharp; shd = shoulder.

All the 13 Raman-active vibrations recognized by [63] or [80] can be observed in our spectra (Table 12, Figure 8). In fact, the factor-group analysis indicates, for scheelite-group structures, a band multiplicity describing a representation of $\Gamma_i = 3A_g + 5B_g + 5E_g$ (13 vibrational modes), from which 7 are internal [stretching ν_1 (A_g); ν_3 (B_g) and ν'_3 (E_g); bending $\nu_2(A_g)$, $\nu'_2(B_g)$, $\nu_4(B_g)$ and $\nu'_4(E_g)$] and 6 are external (2 rotations, i.e., A_g and E_g, and 4 translations, i.e., $2B_g$ and 2 E_g): [70,73,75,81]. A fourteen-band, detected by us at 883 or 893 cm^{-1} (Table 12), is normally Raman inactive but was also observed by [78] and assumed to be strain-induced ν'_1 (B_g) symmetric stretching.

As a characteristic feature, the Raman spectrum displays an intense band at ~911 cm^{-1}, attributed to the ν_1 symmetric stretching vibration of the WO_4 tetrahedra (Table 12) and identified at 909 cm^{-1} by [77] and [78], at 910 cm^{-1} by [74], at 911 cm^{-1} by [76], and

at 916 cm^{-1} by [70]. The frequency of this band decreases with the progression of the Mo-for-W or Pb-for Ca substitutions [75,76].

The presence of two components of one ν_2 mode cannot be clearly observed because they probably overlap. A closer inspection of the mode located near 400 cm^{-1} allows us to conclude that it is indeed a double mode, as very weak additional bands or shoulders occur in its case (Figure 8).

The low-frequency translational E_g and B_g modes occur at 85 cm^{-1} and overlap [80].

A band located at ~695 cm^{-1} can be observed in all the Raman spectra in Figure 8. This band, which doesn't pertain to scheelite, can be assumed to be the O-W-O antisymmetric stretching in hydrotungstite [82]. Another band, not reproduced in Figure 8 and Table 12 and located at ~1092 cm^{-1}, was recorded in all but five of our Raman spectra and materializes the ν_1 symmetric stretching of the $(CO_3)^{2-}$ groups in the admixed calcite [83].

10. Genetic Considerations

Most tungsten deposits, including tungsten skarns, are typically associated with evolved A- or S-type granites. The three analyzed Romanian deposits, not included among the 203 worldwide W-skarn deposits identified by [25], can be defined and classified as Cu-W skarn deposits. As well as the "true" W-skarns described by [25], they associate with calc-alkaline equigranular plutons in an orogenic belt (i.e., BMMB).

In our specific case, tungsten mineralization is typically associated with fractionated felsic magmas that form under slightly oxidized to reduced fO_2 conditions [84]. In all three cases, the analyzed scheelite samples have low powellite (Mo) contents and are locally associated with molybdenite, which implies that they formed in a reduced environment [85,86]. Associated granodiorites pertain to the ilmenite series of I-type granites as defined by [87], which solidify under reducing conditions, differing from magnetite series magmas [87]. Sulfur in a reduced magma is kept in the silicate melt, whereas sulfur in an oxidized magma escapes to the aqueous phase [88]. The associated scheelite and sulfide-bearing deposits described in this paper seem to be genetically connected with the reducing nature of the ilmenite series granitic magma, as in part of similar Japanese deposits described by [89]. The ore-forming fluid is initially related to the magmatic fluid, particularly to the exolution and segregation of a hydrothermal fluid phase, which can afterwards mix with metamorphic or meteoric waters ([56] and references therein). The low Mo contents in the analyzed samples are compatible with a reducing environment; however, fluctuating Eh conditions may be evident. Mo migrates as Mo^{6+} in oxidizing conditions; thus, Mo substitution is likely to occur in oxidizing environments [90]. This is consistent with thermodynamic calculations, which indicate that scheelite and molybdenite exhibit an overlapping field of stability in terms of oxygen and sulfur fugacities under normal skarn system conditions [45,85].

The hosting skarns are formed at relatively low temperature (up to 600 °C) and pressure (up to 3 kbar according to [32]) in a reducing environment. Scheelite, however, appears to crystallize from late hydrothermal solutions during a retrograde stage of skarn evolution. At Ciclova and Oravița, the mineralizing solutions may have been supplied through original fissures, which were later filled with late quartz and calcite veins in tourmaline-rich endoskarns [15]. At Băița Bihor, scheelite-rich bands occur in the mass of diopside- and chondrodite + norbergite-rich magnesian skarn at the limit of the outer, borate-bearing zone of the metasomatic columns. In all three occurrences, fluorite occurs as micrometer- to millimeter-sized individual anhedral crystals (Figure 9), sometimes associated with scheelite, which is not unusual as it was also described in other scheelite occurrences throughout the world (e.g., [11,45,47,55,56,89]). Conversely, boron-bearing minerals (i.e., schorlite at Ciclova and Oravița and magnesian borates at Băița Bihor) are particularly abundant in the scheelite-bearing skarns.

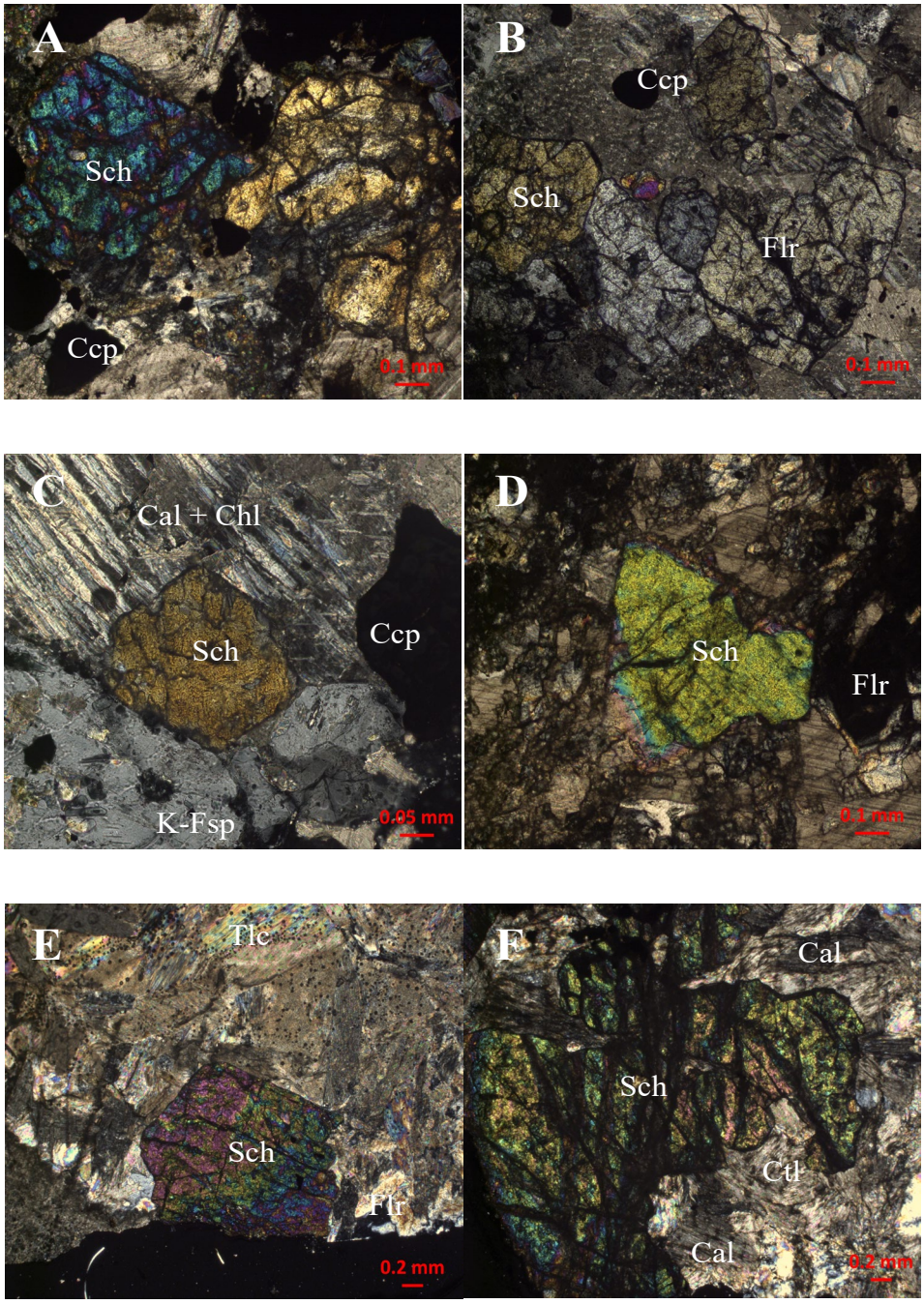

Figure 9. Photomicrographs showing characteristic relationships between scheelite and associated skarn minerals. Crossed polars. (**A**) Crystals of scheelite (Sch) associated with chalcopyrite (Ccp) in the calcite (Cal) mass. Sample 2506 Ciclova. (**B**) Crystals of scheelite (Sch) associated with chalcopyrite (Ccp) and fluorite (Flr). Sample 2575 Ciclova. (**C**) Crystals of scheelite (Sch) and chalcopyrite (Ccp) surrounded by calcite + chlorite (Cal + Chl) and adularia (K-Fsp). Sample 2537 Oravița. (**D**) Aggregate of scheelite (Sch) crystals associated with fluorite (Flr) in the calcite mass. Sample 2569 Oravița. (**E**) Crystal of scheelite (Sch) surrounded by carbonates (calcite, dolomite) and talc (Tlc). Sample 2544 Băița Bihor. (**F**) Aggregate of scheelite (Sch) crystals surrounded by calcite (Cal) and chrysotile (Ctl). Sample 2593 Băița Bihor. Abbreviations of mineral species after [91].

These observations suggest that W was introduced in the skarn system by fluoride-bearing aqueous fluids at relatively low temperatures and vapor-saturated water pressure (e.g., as per experimental conditions used by [92]). Accepting that these experimental conditions were fulfilled during the hydrothermal evolution of the skarn systems described in this paper, we must accept that tungsten was dissolved predominantly as $H_3WO_4F^{2-}$ in

solutions containing 0.05–0.30 m HF at pH (T) values between 1.5 and 3.4 and temperatures between 100 and 250 °C. The occurrence of abundant fluorite in scheelite-bearing samples from quartz-vein deposits from Ciclova and Oravița supports the hypothesis of scheelite crystallization from F-bearing fluids. The ideal reaction to form both scheelite and fluorite may be written, in our case, as: $2\ H_3WO_4F^{2-} + 3\ CaCO_3 = 2\ CaWO_4 + CaF_2 + 3\ H_2CO_3$.

Alternatively, a number of authors (e.g., [93] and referred works) showed that a large amount of boron can be dissolved in F-bearing hydrothermal solutions, which implies that speciation of B-bearing minerals is possible in similar conditions as for scheelite and explains the presence of boron minerals in the W-bearing skarns at Ciclova, Oravița, and Băița Bihor.

11. Conclusions

Physical and crystallographic properties and vibrational behavior, as well as crystal chemistry, show that scheelite from Ciclova, Oravița, and Băița Bihor is close to stoichiometry.

In all cases, the analyzed samples show, at least locally, oscillatory zonation in cathodoluminescence, characteristic of scheelite from proximal intrusion-related systems such as skarns. CL peculiarities suggest that, in the analyzed occurrences, scheelite formation was controlled by multiple factors, e.g., the nature of ore-forming fluids and crystal diffusion or growth rate. In all cases, the CL images of the crystals vary from homogenous to zoned, behaving like hydrothermal scheelite and suggesting slight oscillations in the Eh of the crystallizing solutions, from slightly oxidizing to reducing. Textural relations and petrographic evidence indicate that the analyzed scheelite crystallizes late in the skarn paragenesis, apparently from epigenetic hydrothermal fluids.

Scheelite described in this paper is typically associated with hydrous minerals and retrograde alteration but also with F- and B-bearing minerals, suggesting that the mineral crystallized from epithermal, low-temperature fluoride- and boron-bearing aqueous solutions.

The Ciclova, Oravița, and Băița Bihor deposits in Romania can be defined as Cu-W skarns but also contain significant contents of other metals (i.e., Pb, Zn, Bi, Mo, Ag, and Au). At least the deposit from Băița Bihor, which is a quite important source of Cu, Mo, and base metals, can produce a significant amount of byproduct W.

Supplementary Materials: The following supporting information can be downloaded at: https://www.mdpi.com/article/10.3390/min15080854/s1, Word-transposed *.cif files with structure data for representative samples of scheelite from Ciclova (Sample 2509), Oravița (Sample 2538) and Băița Bihor (Sample 2544).

Author Contributions: Conceptualization, Ş.M., D.-G.D., F.H. and M.D.; formal analysis, Ş.M., C.S.G., D.-G.D., M.D., F.H., G.D. and G.C.; funding acquisition, Ş.M., D.-G.D., C.S.G., A.-M.I., G.C. and F.H.; investigation, Ş.M., D.-G.D., F.H., C.S.G., M.D., G.D. and G.C.; methodology, Ş.M., D.-G.D., G.C. and F.H.; resources, Ş.M., D.-G.D., F.H., G.C. and C.S.G.; data curation, Ş.M., D.-G.D., C.S.G., F.H. and M.D.; writing—original draft preparation, Ş.M.; writing—review and editing, Ş.M.; visualization, Ş.M.; supervision, Ş.M.; project administration, Ş.M., D.-G.D., C.S.G. and F.H. All authors have read and agreed to the published version of the manuscript.

Funding: This study was partly supported by two scientific cooperative research grants awarded by the Walloon and Romanian Governments (4 BM/2021 and 1BCBE/2024). Other grants allowed to the first author by UEFISCDI in Romania (PN-III-P1-1.2-PCCDI-2017-0346 and PN-III-P1-1.1-MC-2018-3163) and by the Ministry of Education and Research (PN23-39-02-01/2023, PN23-39-02-06/2023 and PN23-39-02-07/2023) generously supported the final draft. C.S.G and A.-M.I. gratefully acknowledge the receipt of two UEFISCDI grant (PN-III-P1-1.1-MC-2018-3199 and PN-III-P1-1.1-MC-2018-3211) which helped to obtain part of the structural data.

Data Availability Statement: Primary data presented in this study are available on request from the first author. More data for structure refinements, including *.cif files, are available on request from the fifth author (fhatert@uliege.be).

Acknowledgments: The use of the EPMA facility at the Department of Earth, Environmental, and Planetary Sciences, Rice University, Houston, Texas, is kindly acknowledged. The assistance of Gabriela Stelea (Geological Institute of Romania, Bucharest) in the acquisition of the infrared spectra is gratefully acknowledged. Corentin Amador del Valle (University in Liège) kindly communicated some of the XRD and EMP analyses used for this study. Fruitful discussions on the field with the late Jean Verkaeren, with André-Mathieu Fransolet, Bernard Guy, Essaïd Bilal, Gheorghe Ilinca, Jacqueline Vander Auwera, Hans-Peter Schertl, Walter Maresh, Evgheny Galuskin, Irina Galuskina, Robert Martin and Maxime Baijot were highly appreciated. Members of the staffs of SC Băița Bihor SA and Vast Resources PLC-Băița Plai mining companies are gratefully acknowledged for their assistance in the sampling activities. The authors are grateful to Alexandru Călin and to the Academic Editor for handling the manuscript, as well as to three anonymous referees for their thorough reviews of an earlier draft.

Conflicts of Interest: The authors declare no conflicts of interest.

References

1. British Geological Survey. Tungsten. In *British Geological Survey*; BGS: Keyworth, UK, 2011; pp. 1–34.
2. Yang, X. Beneficiation studies of tungsten ores—A review. *Min. Eng.* **2018**, *125*, 111–119. [CrossRef]
3. Han, Z.; Golev, A.; Edraki, M.A. Review of tungsten resources and potential extraction from mine waste. *Minerals* **2021**, *11*, 701. [CrossRef]
4. Grohol, M.; Veeh, C. *Study on the Critical Raw Materials for the EU 2023*; DG Grow, European Commission, Luxembourg Publication Office of the EU: Luxembourg, 2023; pp. 1–152.
5. Rowan, L.R. *Critical Mineral Resources: National Policy and Critical Minerals List*; Congressional Research Service Report: CRS Report R47982 2025; Library of Congress: Washington, DC, USA, 2025; pp. 1–22.
6. Hocquard, C. Les nouveaux métaux stratégiques: Métaux high-tech, «métaux verts», métaux stratégiques, vers une convergence. *Mag'Mat* **2008**, *26*, 1–30.
7. Liu, Y.; Jia, D.; Zhou, Y.; Zhou, Y.; Zhao, J.; Li, Q.; Liu, B. Discovery of ABO_4 scheelites with the extra low thermal conductivity through high-throughput calculations. *J. Mater.* **2020**, *6*, 702–711. [CrossRef]
8. Li, S.; Bychkov, K.L.; Butenko, D.S.; Terebilenko, K.V.; Zhu, Y.; Han, W.; Baumer, V.N.; Slobodyanik, M.S.; Ji, H.; Klyui, N.I. Scheelite-related $M^{II}_xBi_{1-x}V_{1-x}Mo_xO_4$ (M^{II}—Ca, Sr) solid solution-based photoanodes for enhanced photoelectrochemical water oxidation. *Dalton Trans.* **2020**, *49*, 2345–2355. [CrossRef]
9. Shivakumar, C.; Saraf, R.; Behera, S.; Dhananjaya, N.; Nagabhushana, H. Scheelite-type MWO_4 (M = Ca, Sr, and Ba) nanophosphors: Facile synthesis, structural characterization, photoluminescence, and photocatalytic properties. *Mater. Res. Bull.* **2015**, *61*, 422–432. [CrossRef]
10. Potanina, E.A.; Orlova, A.I.; Mikhailov, D.A.; Nokhrin, A.V.; Chuvil'deev, V.N.; Boldin, M.S.; Sakharov, N.V.; Lantcev, E.A.; Tokarev, M.G.; Murashov, A.A. Spark Plasma Sintering of fine-grained $SrWO_4$ and $NaNd(WO_4)_2$ tungstates ceramics with the scheelite structure for nuclear waste immobilization. *J. Alloys Compd.* **2019**, *774*, 182–190. [CrossRef]
11. Liu, X.; Yang, J.; Chen, Q. Study on spectral characteristics and color origin of scheelite from Xuebaoding, Pingwu County, Sichuan Province, P.R. China. *Minerals* **2022**, *12*, 1344. [CrossRef]
12. Cao, Q.; Shi, M.; Yuan, Y.; Ma, S.; Lu, H. Mineralogy and geochemical characteristics of scheelite deposit at Xuebaoding in Pingwu, Sichuan Province, China. *Minerals* **2024**, *14*, 38. [CrossRef]
13. Koch, A. Űber den Vesuvian und Scheelit von Csiklova. *Földtany Közlöny* **1924**, *54*, 85–90.
14. Superceanu, C. New occurrences of scheelite in contact deposits from the Banatitic geochemical province. *Rev. Min.* **1956**, *4–5*, 230–234. (In Romanian)
15. Constantinescu, E.; Ilinca, G.; Ilinca, A. Laramian hydrothermal alteration and ore deposition inthe Oravița—Ciclova area, South–western Banat. *D. S.—Inst. Geol. Geofiz.* **1988**, *72–73*, 13–26.
16. Cioflică, G.; Vlad, Ş.; Iosof, A.; Panican, A. Scheelite occurrences in the Bihor Massif. *Rev. Roum. Géol. Géoph. Géogr.* **1976**, *20*, 169–177.
17. Berza, T.; Constantinescu, E.; Vlad, Ş.N. Upper Cretaceous magmatic series and associated mineralization in the Carpatho-Balkan Orogen. *Res. Geol.* **1998**, *48*, 291–306. [CrossRef]

18. Cioflică, G.; Vlad, Ş. The correlation of the Laramian metallogenetic events belonging to the Carpatho-Balkan area. *Rev. Roum. Géol. Géophys. Géogr. Sér. Géol.* **1973**, *17*, 217–224.
19. Ciobanu, C.L.; Cook, N.J.; Stein, H. Regional setting and geochronology of the Late Cretaceous Banatitic Magmatic and Metallogenetic Belt. *Miner. Depos.* **2002**, *37*, 541–567. [CrossRef]
20. Zimmermann, A.; Stein, H.; Hannah, J.; Koželj, D.; Bogdanov, K.; Berza, T. Tectonic configuration of the Apuseni—Banat—Timok—Srednogorie belt, Balkans–Southern Carpathians, constrained by high precision Re–Os molybdenite ages. *Miner. Depos.* **2008**, *43*, 1–21. [CrossRef]
21. Ilinca, G. Classic skarn localities of Romania: Contact metamorphism and mineralization related to Late Cretaceous magmatism. *Acta Min.-Petr.* **2010**, *23*, 1–50.
22. Ilinca, G. Upper Cretaceous contact metamorphism and related mineralizations in Romania. *Acta Min.-Petr. Abstr. Ser.* **2012**, *7*, 59–64.
23. Vlad, Ş.N. Banatite metallogeny of North Poiana Ruscă Mts. Revisited. *Geol. Anali Balkanskoga Poluostrva* **2020**, *81*, 67–77. [CrossRef]
24. Săndulescu, M.; Kräutner, H.; Borcoş, M.; Năstăseanu, S.; Patrulius, D.; Ştefănescu, M.; Ghenea, C.; Lupu, M.; Savu, H.; Bercia, I.; et al. *Geological Map of Romania, scale 1:1,000,000*; Institute of Geology and Geophysics: Bucharest, Romania, 1978.
25. Meinert, L.D.; Dipple, G.M.; Nicolescu, Ş. World skarn deposits. In *Economic Geology 100th Anniversary Volume*; Society of Economic Geologists: Littleton, CO, USA, 2005; pp. 299–336.
26. Soroiu, M.; Catilina, R.; Strutinski, C. K-Ar ages on some igneous rocks from the southwestern end of the South Carpathians (Banat Hills). *Rev. Roum. Phys.* **1986**, *31*, 849–854.
27. Gallhofer, D. Magmatic Geochemistry and Geochronology in Relation to the Geodynamic and Metallogenetic Evolution of the Banat Region and Apuseni Mountains of Romania. Ph.D. Thesis, ETH Zürich, Zürich, Switzerland, 2015. Dissertation ETH no 22888. pp. 1–45.
28. Bleahu, M.; Soroiu, M.; Catilina, R. On the Cretaceous tectonic-magmatic evolution of the Apuseni Mountains as revealed by K-Ar dating. *Rev. Roum. Phys.* **1984**, *29*, 123–130.
29. Pavelescu, L.; Pop, G.O.; Weisz, E.; Popescu, G. La nature et l'âge du batholite banatitique de Bihor. *Rep. XII-th Congress K.B.G.A. Cracow* **1985**, 98–101.
30. Cioflică, G.; Jude, R.; Lupulescu, M. Cupriferous metallization processes associated with Upper Cretaceous–Eocene magmatites from Romania. *Rom. J. Mineral.* **1992**, *76*, 1–16.
31. Vlad, Ş.N. Calcic skarns and transversal zoning in the Banat Mountains, Romania: Indicators of an Andean–type setting. *Miner. Depos.* **1997**, *32*, 446–471. [CrossRef]
32. Marincea, Ş.; Dumitraş, D.-G. Contrasting types of boron-bearing deposits in magnesian skarns from Romania. *Ore Geol. Rev.* **2019**, *112*, 102952. [CrossRef]
33. Cioflică, G.; Vlad, Ş.; Stoici, S. Repartition de la mineralization dans le skarn de Băiţa Bihorului. *Rev. Roum. Géol. Géoph. Géogr.* **1971**, *15*, 43–58.
34. Tămaş, C.G.; Andrii, M.-P. Mineralogy of skarn ores from Băiţa Bihor, Northern Apuseni Mountains, Romania: A case study of Cu-, Bi- and Sn-minerals. *Minerals* **2020**, *10*, 436. [CrossRef]
35. Armstrong, J.T. Quantitative analysis of silicates and oxide minerals: Comparison of Monte Carlo, ZAF and Phi-Rho-Z procedures. In *Microbeam Analysis*; Newbury, D.E., Ed.; San Francisco Press: San Francisco, CA, USA, 1988; pp. 239–246.
36. Appleman, D.E.; Evans, H.T., Jr. Indexing and least-squares refinement of powder diffraction data. *U.S. Geol. Surv. Comput. Contrib.* **1973**, *20*, 60.
37. Benoit, P.H. Adaptation to microcomputer of the Appleman-Evans program for indexing and least-squares refinement of powder-diffraction data for unit-cell dimensions. *Am. Mineral.* **1987**, *72*, 1018–1019.
38. Kalinkina, E.V.; Kalinkin, A.M.; Forsling, W.; Makarov, A.M. Sorption of atmospheric carbon dioxide and structural changes of Ca and Mg silicate minerals during grinding. II. Enstatite, åkermanite and wollastonite. *Int. J. Miner. Process.* **2001**, *61*, 289–299. [CrossRef]
39. Agilent Technologies. *Xcalibur CCD System, CrysAlis Software System*; Agilent Technologies: Oxfordshire, UK, 2012.
40. Palatinus, L.; Chapuis, G. Superflip—A computer program for the solution of crystal structures by charge flipping in arbitrary dimensions. *J. Appl. Crystallogr.* **2007**, *40*, 786–790. [CrossRef]
41. Petříček, V.; Dušek, M.; Palatinus, L. Crystallographic computing system Jana2006: General features. *Z. Kristallogr.* **2014**, *229*, 345–352. [CrossRef]
42. Xu, J.; Ciobanu, C.L.; Cook, N.; Slattery, A. Crystals from the powellite-scheelite series at the nanoscale: A case study from the Zhibula Cu skarn, Gangdese Belt, Tibet. *Minerals* **2019**, *9*, 340. [CrossRef]
43. Wen, J.; Zheng, S.; Chu, X.; Jiang, H.; Zhao, Y. Mineralogical characteristics of scheelite in the Xi'an tungsten deposit, western Hunan. *IOP Conf. Ser. Earth Env. Sci.* **2021**, *658*, 012044. [CrossRef]

44. Ilinca, G.; Marincea, Ş. Hydrotungstite from Oraviţa-Ciclova and Băiţa Bihor: The first occurrences in Romania. *Rom. J. Mineral.* **1993**, *76* (Suppl. S1), 24–25.
45. Poulin, R.S.; McDonald, A.M.; Kontak, D.J.; McClenaghan, M.B. On the relationship between cathodoluminescence and the chemical composition of scheelite from geologically diverse ore-deposit environments. *Can. Mineral.* **2016**, *54*, 1147–1173. [CrossRef]
46. Xiao, X.; Zhou, T.; Shi, K.; White, N.C.; Fan, Y.; Wang, F.; Chen, X. Trace elements and textures of scheelite in porphyry-skarn Cu-Au systems: The example of Dongguashan deposit, eastern China. *Ore Geol. Rev.* **2022**, *149*, 105069. [CrossRef]
47. Miranda, A.C.R. Chemical Composition of Scheelite and its Application as An Indicator Mineral. Ph.D. Thesis, Laval University, Québec, QC, Canada, 2023; pp. 1–459.
48. Kay, M.I.; Frazer, B.C.; Almodovar, I. Neutron diffraction refinement of $CaWO_4$. *J. Chem. Phys.* **1964**, *40*, 504–506. [CrossRef]
49. Blanchard, F. X-ray powder data for $CaWO_4$, synthetic scheelite. *Powder Diffr.* **1989**, *4*, 220–222. [CrossRef]
50. Sleight, A.W. Accurate cell dimensions for ABO_4 molybdates and tungstates. *Acta Cryst.* **1972**, *28*, 2899–2902. [CrossRef]
51. Senyshyn, A.; Kraus, H.; Mikhailik, V.B.; Yakovyna, V. Lattice dynamics and thermal properties of $CaWO_4$. *Phys. Rev.* **2004**, *70*, 214306. [CrossRef]
52. Hazen, R.M.; Finger, L.W.; Mariathasan, J.W. High-pressure crystal chemistry of scheelite-type tungstates and molybdates. *J. Phys. Chem Solids* **1985**, *46*, 253–263. [CrossRef]
53. Rabuffetti, F.A.; Culver, S.P.; Suescun, L.; Brutchey, R.L. Structural disorder in $AMoO_4$ (A = Ca, Sr, Ba) scheelite nanocrystals. *Inorg. Chem.* **2014**, *53*, 1056–1061. [CrossRef]
54. Shoji, T.; Sasaki, N. Fluorescent color and X-ray powder data of synthesized scheelite- powellite series as guides to determine its composition. *Min. Geol.* **1978**, *28*, 397–404.
55. Palmer, M.C. Geochemical Characterisation of Scheelite from New Zealand. Ph.D. Thesis, Otago University, Dunedin, New Zealand, 2021; pp. 1–220.
56. Lu, D.; Mao, J.; Ye, H.; Wang, P.; Chao, W.; Yu, M. Geochemistry of scheelite from Jiangligou skarn W-(Cu-Mo) deposit in the West Qinling orogenic belt, Northwest China: Implication on the multistage ore-forming processes. *Ore Geol. Rev.* **2023**, *159*, 105525. [CrossRef]
57. Palache, C.; Berman, H.; Frondel, C. *The System of Mineralogy. II. Halides, Nitrates, Borates, Carbonates, Sulfates, Phosphates, Arsenates, Tungstates, Molybdates, etc.*; John Wiley and Sons: New York, NY, USA, 1951; pp. 1–1124.
58. Mandarino, J.A. The Gladstone-Dale relationship—Part I: Derivation of new constants. *Can. Mineral.* **1976**, *14*, 498–502.
59. Zalkin, A.; Templeton, D.H. X-ray diffraction refinement of the calcium tungstate structure. *J. Chem. Phys.* **1964**, *40*, 501–504. [CrossRef]
60. Mandarino, J.A. The Gladstone-Dale relationship. IV. The compatibility concept and its application. *Can. Mineral.* **1981**, *19*, 441–450.
61. Larsen, E.S. The microscopic determination of the nonopaque minerals. *U.S. Geol. Surv. Bull.* **1921**, *679*, 1–289.
62. Brown, I.D.; Altermatt, D. Bond-valence parameters obtained from a systematic analysis of the Inorganic Crystal Structure Database. *Acta Cryst. B* **1985**, *41*, 244–247. [CrossRef]
63. Barker, A.S. Infrared lattice vibrations in calcium tungstate and calcium molybdate. *Phys. Rev. A* **1964**, *135*, 742–747. [CrossRef]
64. Clark, G.M.; Doyle, W.P. IR spectra of anhydrous molybdates and tungstates. *Spectrochim. Acta* **1966**, *22*, 1441–1447. [CrossRef]
65. Khanna, R.K.; Lippincott, E.R. Infrared spectra of some scheelite structures. *Spectrochim. Acta A* **1968**, *24*, 905–908. [CrossRef]
66. Zorina, M.L.; Syritso, L.F. IR spectra and structures of tungstates. *J. Appl. Crystallogr.* **1972**, *16*, 774–776. [CrossRef]
67. Tarte, P.; Liegeois-Duyckaerts, M. Vibrational studies of molybdates, tungstates and related compounds—I. New infrared data and assignments for the scheelite-type compounds $X^{II}MoO_4$ and $X^{II}WO_4$. *Spectrochim. Acta A* **1972**, *28*, 2029–2036. [CrossRef]
68. Iishi, K. Study of the force field of scheelite. *Z. Kristallogr.* **1975**, *141*, 31–58. [CrossRef]
69. Zhou, P.L. Infrared spectra of wolframite and scheelite from tungsten ore deposits in Southern Ganzhou, Jiangxi Province. *Acta Mineral. Sinca* **1984**, *4*, 319–322.
70. Akimov, A.N.; Nikanovich, M.V.; Popov, V.G.; Umreiko, D.S. Calculation and investigation of the vibrational spectra of scheelite structures $MeWO_4$ (Me = Ca, Sr, Ba, Pb). *Zh. Prikladn. Spektr.* **1986**, *45*, 225–232. (In Russian) [CrossRef]
71. Chukanov, N.V. *Infrared Spectra of Mineral Species. Extended Library*; Springer Geochemistry/Mineralogy: Berlin/Heidelberg, Germany, 2014; pp. 1–1726.
72. Russell, J.P.; Loudon, R. The first-order Raman spectrum of calcium tungstate. *Proc. Phys. Soc.* **1965**, *85*, 1029–1033. [CrossRef]
73. Porto, S.P.S.; Scott, J.F. Raman Spectra of $CaWO_4$, $SrWO_4$, $CaMoO_4$, and $SrMoO_4$. *Phys. Rev.* **1967**, *157*, 716–721. [CrossRef]
74. Griffith, W.P. Raman studies on rock-forming minerals. Part II. Minerals containing MO_3, MO_4, and MO_6 groups. *J. Chem. Soc. A* **1970**, *2*, 286–291. [CrossRef]
75. Liegeois-Duyckaerts, M.; Tarte, P. Vibrational studies of molybdates, tungstates and related compounds—II. New Raman data and assignments for the scheelite-type compounds. *Spectrochim. Acta A* **1972**, *28*, 2037–2051. [CrossRef]

76. Basiev, T.T.; Sobol, A.A.; Voronko, Y.K.; Zverev, P.G. Spontaneous Raman spectroscopy of tungstate and molybdate crystals for Raman lasers. *Opt. Mater.* **2000**, *15*, 205–216. [CrossRef]
77. Crane, M.; Frost, R.L.; Williams, P.A.; Kloprogge, J.T. Raman spectroscopy of the molybdate minerals chillagite (tungstenian wulfenite-I4), stolzite, scheelite, wolframite and wulfenite. *J. Raman Spectrosc.* **2002**, *33*, 62–66. [CrossRef]
78. Frost, R.L.; Duong, L.; Weier, M. Raman microscopy of selected tungstate minerals. *Spectrochim. Acta A Mol. Biomol. Spectrosc.* **2004**, *60*, 1853–1859. [CrossRef]
79. Müller, A.; Krebs, B. Normal coordinate treatment of XY_4-type molecules and ions with T_d symmetry. Part I. Force constants of a modified valence force field and of the Urey-Bradley force field. *J. Molec. Spectr.* **1967**, *24*, 180–197. [CrossRef]
80. Khanna, R.K.; Brower, W.S.; Guscott, B.R.; Lippincott, E.R. Laser induced Raman spectra of some tungstates and molybdates. *J. Res. Nat. Inst. Stand. Techn. Phys. Chem. A* **1968**, *72*, 81–84. [CrossRef]
81. Kanamori, H.; Hayashi, S.; Ikeda, Y.Y. External lattice vibration modes in scheelites. *J. Phys. Soc. Jap.* **1974**, *36*, 511–516. [CrossRef]
82. Daniel, M.F.; Desbat, B.; Lassegues, J.C.; Gerand, B.; Figlarz, M. Infrared and Raman study of $WO_3 \cdot xH_2O$ tungsten trioxide hydrates. *J. Solid State Chem.* **1987**, *67*, 235–247. [CrossRef]
83. Gunasekaran, S.; Anbalagan, G.; Pandi, S. Raman and infrared spectra of carbonates of calcite structure. *J. Raman Spectr.* **2006**, *37*, 892–899. [CrossRef]
84. Newberry, R.; Swanson, S. Scheelite skarn granitoids: An evaluation of the roles of magmatic source and process. *Ore Geol. Rev.* **1986**, *1*, 57–81. [CrossRef]
85. Hsu, L.C.; Galli, P. E, Origin of the scheelite-powellite series of minerals. *Econ. Geol.* **1973**, *68*, 681–696. [CrossRef]
86. Hsu, L.C. Effects of oxygen and sulfur fugacities on the scheelite-tungstenite and powellite-molybdenite stability relations. *Econ. Geol.* **1977**, *72*, 664–670. [CrossRef]
87. Ishihara, S. The magnetite-series and ilmenite-series granitic rocks. *Mining Geol.* **1977**, *27*, 293–305.
88. Ishihara, S. The granitoid series and mineralization. In *Economic Geology 75th Anniversary Volume*; The Economic Geology Publishing Company: Littleton, CO, USA, 1981; pp. 458–484.
89. Sato, K. Tungsten skarn deposit of the Fujigatani Mine, Southwest Japan. *Econ. Geol.* **1980**, *75*, 1066–1082. [CrossRef]
90. Song, G.X.; Qin, K.Z.; Li, G.; Evans, N.J.; Chen, J. Scheelite elemental and isotopic signatures: Implication for the genesis of skarn-type W-Mo deposits in the Chizhou area, Anhui Province, eastern China. *Amer. Miner.* **2014**, *99*, 303–317. [CrossRef]
91. Warr, L.N. IMA-CNMNC approved mineral symbols. *Min. Mag.* **2021**, *85*, 291–320. [CrossRef]
92. Wang, X.-S.; Williams-Jones, A.E.; Hu, R.Z.; Lin-Bo, S.; Xian-Wu, B. The role of fluorine in granite-related hydrothermal tungsten ore genesis: Results of experiments and modelling. *Geochim. Cosmochim. Acta* **2021**, *292*, 170–187. [CrossRef]
93. Qiu, Y.; Zhang, R.; Chou, I.-M.; Wang, X.; Hu, W.; Zhang, W.; Lu, J.; Li, G.; Li, Z. Boron-rich ore-forming fluids in hydrothermal W-Sn deposits from South China: Insights from in situ Raman spectroscopic characterization of fluid inclusions. *Ore Geol. Rev.* **2021**, *132*, 104048. [CrossRef]